

## Key Points:

- We present the first concurrent observations of ocean pressure and ice flexure in the grounding zone of an Antarctic ice shelf
- Peak ocean pressure in the grounding zone at high tide exceeded glaciostatic pressure and preceded the peak ice shelf tidal deflection
- These pressure variations may enhance basal crevassing and influence subglacial hydrology near the grounding line

## Correspondence to:

C. B. Begeman,  
 cbegeman@lanl.gov

## Citation:








Begeman, C. B., Tulaczyk, S., Padman, L., King, M., Siegfried, M. R., Hodson, T. O., & Fricker, H. A. (2020). Tidal pressurization of the ocean cavity near an Antarctic ice shelf grounding line. *Journal of Geophysical Research: Oceans*, 125, e2019JC015562. <https://doi.org/10.1029/2019JC015562>

Received 11 AUG 2019

Accepted 10 MAR 2020

Accepted article online 16 MAR 2020

# Tidal Pressurization of the Ocean Cavity Near an Antarctic Ice Shelf Grounding Line

Carolyn Branecky Begeman<sup>1,2</sup> , Slawek Tulaczyk<sup>1</sup> , Laurie Padman<sup>3</sup> , Matt King<sup>4</sup> ,  
 Matthew R. Siegfried<sup>5,6</sup> , Timothy O. Hodson<sup>7</sup> , and Helen A. Fricker<sup>6</sup> 

<sup>1</sup>Department of Earth and Planetary Sciences, University of California, Santa Cruz, CA, USA, <sup>2</sup>Fluid Dynamics and Solid Mechanics, Los Alamos National Laboratory, Los Alamos, NM, USA, <sup>3</sup>Earth and Space Research, Corvallis, OR, USA, <sup>4</sup>School of Geography and Spatial Sciences, School of Technology, Environments and Design, University of Tasmania, Hobart, Tasmania, Australia, <sup>5</sup>Institute of Geophysics and Planetary Physics, Scripps Institute of Oceanography, University of California, La Jolla, CA, USA, <sup>6</sup>Department of Geophysics, Colorado School of Mines, Golden, CO, USA, <sup>7</sup>Department of Geology and Environmental Geosciences, Northern Illinois University, DeKalb, IL, USA

**Abstract** Mass loss from the Antarctic ice sheet is sensitive to conditions in ice shelf grounding zones, the transition between grounded and floating ice. To observe tidal dynamics in the grounding zone, we moored an ocean pressure sensor to Ross Ice Shelf, recording data for 54 days. In this region the ice shelf is brought out of hydrostatic equilibrium by the flexural rigidity of ice, yet we found that tidal pressure variations at a constant geopotential surface were similar within and outside of the grounding zone. This implies that the grounding zone ocean cavity was overpressurized at high tide and underpressurized at low tide by up to 10 kPa with respect to glaciostatic pressure at the ice shelf base. Phase lags between ocean pressure and vertical ice shelf motion were tens of minutes for diurnal and semidiurnal tides, an effect that has not been incorporated into ocean models of tidal currents below ice shelves. These tidal pressure variations may affect the production and export of meltwater in the subglacial environment and may increase basal crevasse heights in the grounding zone by several meters, according to linear elastic fracture mechanics. We find anomalously high tidal energy loss at the  $K_1$  constituent in the grounding zone and hypothesize that this could be explained by seawater injection into the subglacial environment at high tide or internal tide generation through interactions with topography. These observations lay the foundation for improved representation of the grounding zone and its tidal dynamics in ocean circulation models of sub-ice shelf cavities.

**Plain Language Summary** One of the challenges for sea level rise prediction is understanding how the Antarctic ice sheets and the Southern Ocean interact. Ocean tides are an important component of this interaction, influencing ice shelf melting and the flow rate of grounded ice toward the coast. We report new observations relevant to this interaction: tidally varying ocean pressures where the ice first goes afloat to become an ice shelf. These tidal ocean pressure variations influence tidal currents below the ice shelf, and we propose that they also push seawater beneath the ice inland of the ice shelf and extend fractures at the ice shelf base. This study identifies tidal processes that may affect melt and fracture near the inland edge of ice shelves, a highly sensitive zone for ice dynamics.

## 1. Introduction

The flow of many marine-terminating ice streams and glaciers in Antarctica and Greenland dynamically responds to ocean tides (see review by Padman et al., 2018). Tidal ice flow variations may be sinusoidal (e.g., Anandakrishnan et al., 2003; Rosier et al., 2017) or consist of short intervals of relatively rapid flow separated by much longer periods of stagnation, a process referred to as “stick-slip” (e.g., Bindshadler, 2003; Zoet et al., 2012). Tides enhance the time-averaged flow rates of some ice streams by up to 10% (Gudmundsson, 2007; Rosier & Gudmundsson, 2018) through the nonlinear effects of grounding line migration (e.g., Brunt et al., 2011; Rosier et al., 2014; Thomas, 2007) and, possibly, by changing subglacial hydrology (e.g., Rosier & Gudmundsson, 2018; Thompson et al., 2014).

Ocean tides also affect sub-ice shelf ocean currents, ocean mixing, and, consequently, ice shelf basal melting (Gwyther et al., 2016; Jourdain et al., 2019; MacAyeal, 1985; Makinson & Nicholls, 1999; Makinson, 2002;

Makinson et al., 2011; Mueller et al., 2012, 2018). Excess basal melting can result in ice shelf thinning that reduces the back stress on ice flow (i.e., reduces “buttressing”), causing increases in ice flow speed (Dupont & Alley, 2005; Goldberg et al., 2018; Pritchard et al., 2012; Reese et al., 2018). Additionally, coupled ice sheet and ocean models that fail to capture the tidal contribution to basal melting may incorrectly tune parameterizations of basal melting, modifying the sensitivity of basal melting to future ocean conditions (Dinniman et al., 2016). Due to tidal influences on ice stream flow and ice shelf melting, predicting the sea level rise contribution from Antarctica requires accurately modeling tidal interactions between ice shelves and the ocean (Dinniman et al., 2016; Jourdain et al., 2019; Padman et al., 2018).

Ice sheet dynamics are highly sensitive to reduced buttressing caused by increased melting near the grounding line, the location where the ice shelf first goes afloat (Goldberg et al., 2018; Reese et al., 2018; Seroussi & Morlighem, 2018). Below most of the area of large ice shelves, tidal currents that contribute to melting can be evaluated from an ocean model that assumes that the ice shelf is in local hydrostatic equilibrium (Padman et al., 2018). Within the grounding zone, however, the ice shelf’s vertical motion is reduced relative to hydrostatic equilibrium by the flexural rigidity of the ice (e.g., Walker et al., 2013). The tidal deflection of the ice shelf transitions over the grounding zone from zero at the grounded side to the full tidal height at some distance seaward of the grounding line, usually a few kilometers (Brunt et al., 2010, 2011; Fricker & Padman, 2006; Rignot, 2006). Furthermore, the hinging motion of the ice shelf in the grounding zone in response to the tide may be delayed by the elastic and viscous properties of ice (Gudmundsson, 2011; Reeh et al., 2000, 2003, their Figure A1). Tidal currents will be influenced by this temporal relationship between tide propagation and ice shelf flexure. However, these flexural phenomena and the paucity of oceanographic observations in grounding zones has prevented a quantitative understanding of tidal dynamics at this critical interface.

Ice motion has been found to contain not only the dominant semidiurnal and diurnal tidal frequencies but also other low- and high-frequency constituents indicative of nonlinear processes (Gudmundsson, 2006; King et al., 2010, 2011; Pedley et al., 1986). It has proven difficult to attribute nonlinear tide constituents to specific nonlinearities in the ice-ocean system. Many processes in this system are nonlinear: ice deformation (Nye, 1953), sliding of grounded ice over the basal substrate (Budd et al., 1979; Minchew et al., 2017; Rosier & Gudmundsson, 2020), drag between ocean currents and the ice shelf (reviewed by Padman et al., 2018), and other shallow-water effects (Pedley et al., 1986). Measurements of spatial variations in nonlinear tide constituents of ice motion have, so far, not been sufficient to determine which underlying nonlinearities are dominant (e.g., King et al., 2010, 2011). Coincident observations of ice motion and ocean pressure may enable better attribution of nonlinear tides to specific processes. The grounding zone, where the water column is thin, may be a particularly fruitful region for the study of shallow-water effects on nonlinear tides.

Tidal ocean pressure perturbations at the grounding line may propagate upstream into the subglacial environment, affecting subglacial water pressures. Pressure perturbations in a subglacial drainage system with high hydraulic conductivity could travel tens of kilometers (Rosier & Gudmundsson, 2016). Subglacial water pressures modulate the basal shear stress of grounded ice (Anandakrishnan et al., 2003; Rosier et al., 2015; Rosier & Gudmundsson, 2016), a primary source of resistance to ice flow. Tidal basal shear stress variations have been hypothesized to explain tidally modulated ice flow (Rosier et al., 2015; Rosier & Gudmundsson, 2016; Thompson et al., 2014). Previous studies have assumed that tidal ocean pressure variations at the grounding line are the same magnitude as hydrostatic pressure variations downstream of the flexure zone (Rosier & Gudmundsson, 2016; Sayag & Worster, 2011, 2013; Tsai & Gudmundsson, 2015), but this had not been observationally verified. Furthermore, if tidal ocean pressure variations at the grounding zone are large relative to the subglacial hydropotential gradient, they may support hydrologic exchange between the subglacial system and the ocean. This hydrologic exchange would likely impact the melt rate distribution in the vicinity of the grounding line (Milillo et al., 2017; Parizek et al., 2013), a sensitive area for ice dynamics.

Tidal ocean pressure perturbations may also influence basal crevasse development in the grounding zone. While more attention has been devoted to surface crevasses than to basal crevasses because of the effectiveness of hydrofracture at the surface (van der Veen, 1998), basal crevasses may be important to the stability of many ice shelves (Jezek, 1984; Luckman et al., 2012; Shepherd et al., 2003). Basal crevasses increase the basal ice area available for melting and modify the local englacial stress field (Khazendar & Jenkins, 2003; Luckman et al., 2012; Sassolas et al., 1996). Basal crevasses are abundant in grounding zones, where flexural stresses and a contrast in basal shear stress across the grounding line are conducive to their formation (Christianson et al., 2016; Jezek & Bentley, 1983). The height of basal crevasses is set by the force balance

between ocean pressure in the crevasse and the stress field in ice (Jimenez & Duddu, 2018; van der Veen, 1998). In most regions of an ice shelf the pressure at the ice shelf base is thought to be glaciostatic and the ocean pressure is hydrostatic such that these forces balance at the ice shelf base. However, in grounding zones where hydrostatic equilibrium does not hold, ocean pressures in the crevasse may exceed glaciostatic pressures in the ice at high tide, propagating crevasses higher into the ice column.

Here, we present the first concurrent observations of ocean pressure and ice flexure in the grounding zone of an ice shelf. Grounding zone ocean pressure may have previously been observed adjacent to an ice rise (a submerged bank on which the ice shelf grounds) of George VI Ice Shelf, but the motion of the ice shelf was not simultaneously observed (Potter et al., 1985; Pedley et al., 1986). In the present study we measured both ocean pressure on a mooring attached to the ice shelf base and ice shelf motion at the surface from January 2015 to March 2015. We then used these data to evaluate the relationship between propagation of the ocean tide in the grounding zone cavity and propagation of the tidal flexural wave in ice. These observations will aid representations of grounding zone tidal dynamics in sub-ice shelf ocean circulation models. Furthermore, our observations of ocean pressure variations in the grounding zone may inform pressure boundary conditions for models representing ice shelf flexure and grounding line migration, subglacial hydrology, and basal crevassing. We examine the frequency content of tidal potential energy losses across the grounding zone and discuss possible dissipation mechanisms. We also present local patterns in nonlinear tide amplitudes and provide recommendations for further observational campaigns to better constrain nonlinear tides.

## 2. Methods

### 2.1. Tidal Variations in Ocean Pressure

We accessed the sub-ice shelf cavity of Ross Ice Shelf 3 km downstream of the grounding line of Whillans Ice Stream (Site GZ19, Figure 1) using hot water drilling (Rack, 2016; Tulaczyk et al., 2014). This site is within the grounding zone as determined by the limits of ice flexure from differential synthetic aperture radar interferometry (Marsh et al., 2016). The ice shelf thickness at the site was  $757 \pm 1$  m, and the ocean cavity was 10 m thick (Begeman et al., 2018). We deployed a sensor string containing a pressure sensor and 30 thermistors on 16 January 2015. The pressure sensor hung 761 m from the ice surface, roughly middepth in the ocean cavity, within a water mass of almost constant potential density (Begeman et al., 2018). The thermistors were distributed throughout the ice shelf with a maximum spacing of 100 m and a minimum spacing of 1 m near the ice shelf bottom. Pressure and temperature data from these sensors were transmitted weekly via the Iridium satellite network to Campbell Scientific Canada's data center, from which they were available for remote download.

For the present study we used one thermistor at the ice shelf surface to analyze surface temperature variations and another thermistor within a meter above the base of the ice shelf to evaluate the timing of borehole closure by freezing. The thermistors were calibrated in a controlled-temperature bath. The accuracy of these thermistors, determined during calibration, was  $\pm 0.2$  °C.

The pressure sensor is a Submersible Level Transmitter VL4313, an absolute ocean pressure sensor that was set to maximum output at a pressure of 800 dbar, with a resulting sensitivity of  $2.45 \text{ mV dbar}^{-1}$ . The sensor has an accuracy of  $\pm 0.25\%$ , corresponding to 1.7 dbar. The instrumental precision is  $4 \times 10^{-4}$  dbar, but the precision of data transmitted and analyzed in this study was about 0.1 dbar due to memory limitations. We collected a time series of instantaneous ocean pressure at 15-min intervals, with one measurement missed every 24 hr for data transmission. By the end of February 2015, power became intermittent, causing identifiable drops in voltage that we filtered from the data set. Data collection ceased on 16 March 2015, resulting in a record length of 54 days after filtering.

For the first 6 days after deployment, the ocean pressure signal showed a temporal trend (Figure 2e) consistent with the timescale for thermal equilibration as recorded by the deepest thermistor in the ice shelf (basal ice temperature not shown). If this initial equilibration does not reflect mean drift but a decline in the sensor system's sensitivity to pressure fluctuations, then the postequilibration sensitivity would be  $2.47 \text{ mV dbar}^{-1}$ , 1% greater than the theoretical sensitivity. Given that this modification is small, we used the theoretical sensitivity of the sensor. If the sensor system is sensitive to temperature, it would respond more strongly to surface temperature fluctuations than ocean temperature fluctuations, as the former are greater in amplitude and affect a greater cable length. We ruled out significant sensitivity to temperature beyond the equilibration period because the sensor response is inconsistent with phase relationships between diurnal

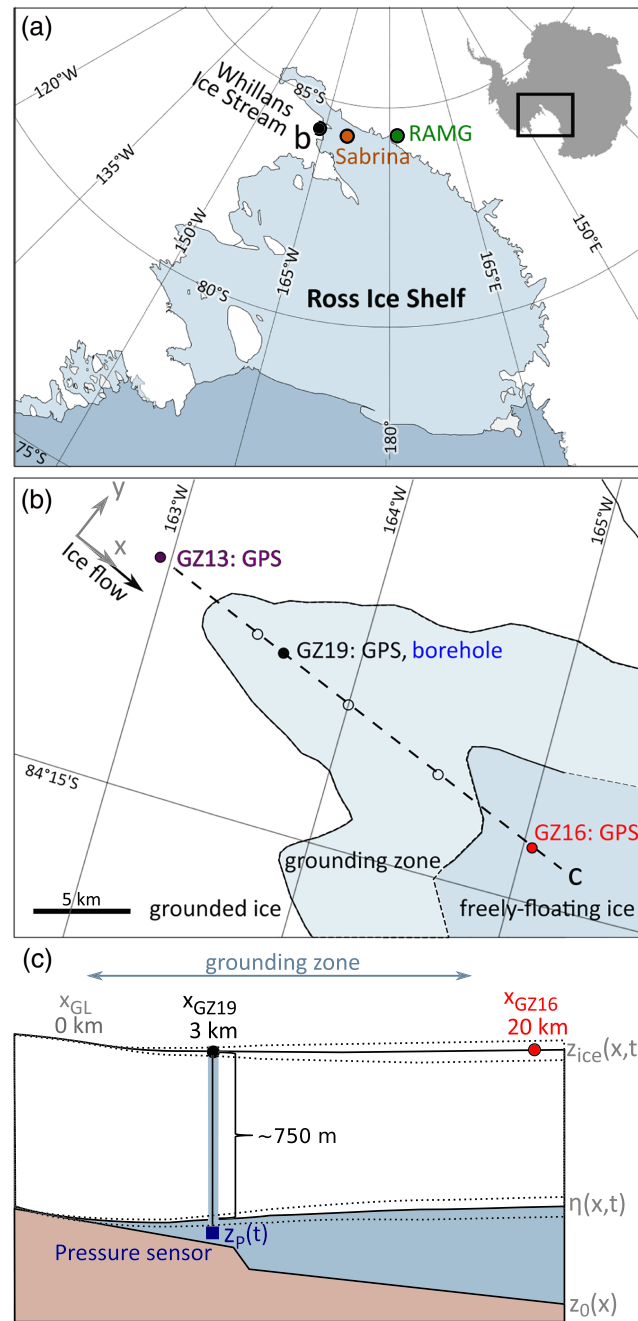


**Figure 1.** (a) Study area on Ross Ice Shelf (black circle). Reference GPS station RAMG (green) and Automatic Weather Station Sabrina (orange). (b) Borehole location and GPS site locations in 2014: GZ19 (black circle); GZ16 (red circle); and GZ13 (purple circle). Empty circles show GPS stations in the region not used in this study (Siegfried et al., 2017, their Figure 1). The grounding zone is bounded using the limits of flexure derived from differential InSAR in 2012 shown with black lines (Marsh et al., 2016). The  $x$  axis defined through the GPS stations (black arrow) is closely aligned with the ice flow direction (gray arrow). (c) Cross section of the ice shelf showing GPS site locations (circles) and pressure sensor (square);  $z_0$  follows the seafloor (bathymetry schematized following Horgan et al., 2013);  $z_{ice}$  denotes the time-varying location of the ice surface and  $\eta$  denotes the time-varying location of the ice base. The origin of the  $x$  axis is defined at the grounding line ( $x_{GL}$ ), and  $x$  increases in the seaward direction. The horizontal blue line shows the extent of the grounding zone.

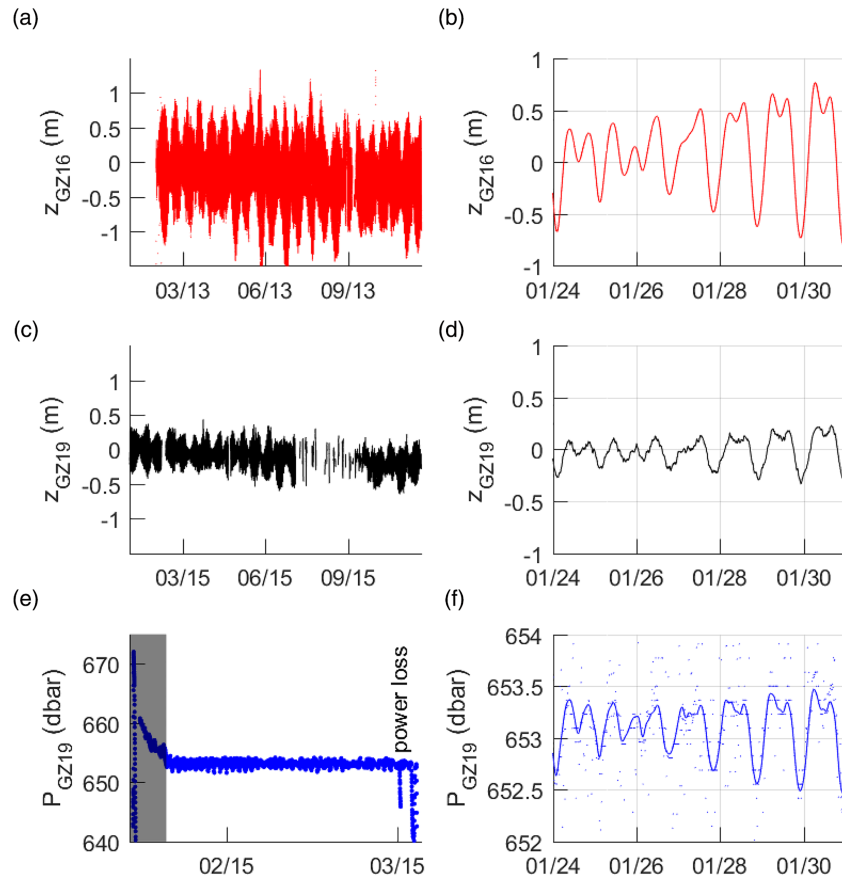


**Figure 2.** Ice shelf deflections at the freely floating station GZ16 for (a) 1 year and (b) 1 week from 2015. Ice shelf deflections at the grounding zone station GZ19 for (c) 1 year and (d) the same week as (b). Ice shelf deflections are computed as the difference from ice shelf height recorded at the start of observations. Ocean pressure in the grounding zone (GZ19) for (e) the full 54-day record (equilibration period shaded in gray) and (f) the same week as (b) and (d). The week of data from the freely floating site (b) is reconstructed over the same time period as the other two measurements.

ocean pressure and diurnal surface temperature measured by the local thermistor (not shown). We excluded the equilibration period from all analyses.

We obtained additional information on ocean pressure variations from two sets of measurements collected concurrently by the Instrumentation Package for Sub-Ice Exploration (IPSIE): pressure measurements from a Seabird 19plus-V2 Conductivity, Temperature, Depth (CTD) sensor, and measurements of sensor distance from the seafloor with a downward facing Tritech altimeter. The minimum range of the altimeter was 2 m; data collected less than 2 m above the seafloor were not analyzed. The precision of these sensors is 0.02 dbar and 1 mm, respectively, and the accuracy of the pressure sensor is 1 dbar. We interpreted some data intervals to have instrumental errors in pressure or depth, based on unphysical step changes in these values.

The IPSIE instrument made a series of traverses through the water column, each lasting on the order of minutes, over a 14-hr period. Since tide height did not change significantly during a single traverse, the pressure evolution during each traverse reflected the time-varying depth of the sensor  $z(t)$

$$p(t) = p_0 - \rho_w g(z(t) - z_0) \quad (1)$$

where  $t$  ranges over the time span of a single traverse. Seawater density,  $\rho_w$ , was well approximated by a constant, the observed depth-averaged in situ seawater density of  $\sim 1,031 \text{ kg m}^{-3}$  (Begeman et al., 2018), and  $p_0$  is the ocean pressure at constant distance from the seafloor ( $z_0$ ). The variation in  $p_0$  between traverses reflected the temporal variation in ocean pressure at a fixed depth. We solved for value of  $p_0$  that produces the best fit (lowest root-mean-square error) for each traverse of the water column and compared the temporal variation in  $p_0$  with tidal deflections at the ice surface as measured by the GPS station at GZ19.



This comparison provided a validation of ocean pressure measurements from the moored sensor and is presented in section 3.3.

## 2.2. Tidal Variations in Ice Shelf Height

We installed continuous dual-frequency GPS systems at two sites, GZ19 and GZ16 (Figure 1). GZ19 was located 284 m seaward of the borehole in the grounding zone, and GZ16 was located 5 km seaward of the outer edge of the zone of ice shelf flexure. We processed GZ19 data from 1 January 2015 to 22 November 2015, a time period that encompasses the collection of ocean pressure data. The GZ16 station was decommissioned before the ocean pressure sensor was installed. For optimal comparison of tidal analyses between the two sites, we used GZ16 data for the same dates, from 1 January to 22 November, but from 2013 instead of 2015. Both of these records span 326 days, although GZ19 had a total of 63 days of data gaps while GZ16 had only 5 days of data gaps; gaps at both stations were due to power loss during polar night.

We processed GPS data kinematically, using Track v1.29 software (Chen, 1998), relative to a reference (static) GPS station (RAMG) located on bedrock 200 km away (Figure 1a). We used final precise satellite orbits from the International Global Navigation Satellite System Service and formed the ionosphere-free linear combination of the two GPS frequencies. Antenna phase-center variations were modeled using igs08\_1884.atx, and solid Earth tides were also modeled. Ocean tide loading displacements were small in this region (submillimeter per constituent) and further reduced through relative processing. Real-valued carrier-phase ambiguity parameters were fixed to integers where possible to minimize synchronization uncertainties between the GPS receiver and the satellite (Remondi, 1985). Site coordinates and tropospheric zenith delays were estimated every measurement epoch (30 s) within the Kalman filter/smoothen implemented in Track. Site coordinates and tropospheric zenith were assigned process noise of 5 mm (30 s)<sup>-1/2</sup> and 0.1 mm (30 s)<sup>-1/2</sup>, respectively (e.g., King & Aoki, 2003). These temporal parameter constraints were chosen to reduce noise while avoiding filtering effects at tidal frequencies including higher harmonics. The short-term (2 min) repeatability of the resulting vertical coordinate time series suggests a precision of 3 cm.

To visualize ice shelf horizontal and vertical deflections across a range of frequencies not limited to standard tidal harmonics, we computed the Lomb-Scargle periodogram for each data set with an oversampling factor of 4. We subsequently applied Gaussian smoothing to each periodogram with a frequency bandwidth of  $5.6 \times 10^{-3}$  Hz (equivalent to a smoothing width of 3 min).

## 2.3. Tidal Constituent Analysis

To extract tidal constituent amplitudes and phases, we used the Matlab software package, Unified Tidal Analysis and Prediction Functions (UTide; Codiga, 2011). UTide was developed from the T\_TIDE package (Pawlowicz et al., 2002) that, in turn, was derived from the FORTRAN code written by Foreman (1977, 1978). The solutions were obtained by an iteratively reweighted least squares approach, which reduces the influence of outliers. Confidence intervals were calculated using a “colored” noise method, based on the spectral properties of the residual, rather than adopting a white noise assumption. The colored noise method results in confidence intervals that are about 30% narrower than under the white noise assumption. Before performing tidal analysis, we bin-averaged the GPS records over 5-min intervals to avoid machine memory limitations. The solution is relatively insensitive to temporal bin width; halving or doubling bin width change amplitude and phase solutions by less than 0.5%.

For tidal constituents with similar frequencies, empirical separation of their amplitudes and phases requires long observational records. Of the tidal constituents shown in Table 1, a minimum of 6 months is needed to separate  $P_1$  from  $K_1$ , and  $K_2$  from  $S_2$  (Foreman, 1977). Since our 54-day ocean pressure record was too short to separate these constituents, we used an inference method (Codiga, 2011). We derived the amplitude ratios and phase offsets for these constituent pairs from the 326-day GZ16 tide solution for 2013, then applied these to the ocean pressure tide solution for 2015. We also calculated the amplitude ratios and phase offsets for GZ16 for 2011, 2012, and 2014 individually to evaluate whether interannual variability influenced the comparison between 2013 and 2015 data.

The  $S_1$  solar tide, which is primarily forced by diurnal atmospheric pressure loading, may be present in oceanographic records (Ray & Egbert, 2004). A yearlong data set is needed to separate  $S_1$  from  $K_1$ . However, the amplitude of  $S_1$  vertical deflections at the freely floating site was small, typically about 2 mm, consistent with the Inverse Barometer Effect (IBE) effect (see section 2.4), evaluated from air pressure at the  $S_1$  frequency at Antarctic Weather Station Sabrina (72 km away, Figure 1a). We ignored the  $S_1$  tide in our analyses

**Table 1**

Major Diurnal and Semidiurnal Tidal Constituents From CATS2008, the Ice Shelf Elevation at Freely Floating Station GZ16, Ice Shelf Elevation at Grounding Zone Station GZ19, and Ocean Pressure at Fixed Distance From the Ice Base Below Grounding Zone Station GZ19 (P)

	$A_{\text{CATS}}$	$\phi_{\text{CATS}}$	$A_{\text{GZ16}}$	$\phi_{\text{GZ16}}$	$A_{\text{GZ19}}$	$\phi_{\text{GZ19}}$	$A_{\text{P}}$	$\phi_{\text{P}}$
$K_1$	44.73	199.77	$45.1 \pm 0.1$	$198.6 \pm 0.1$	$16.2 \pm 0.1$	$206.5 \pm 0.4$	$25 \pm 4^a$	$193 \pm 8^a$
$O_1$	35.90	183.95	$37.6 \pm 0.1$	$182.0 \pm 0.2$	$13.8 \pm 0.1$	$189.1 \pm 0.4$	$25 \pm 1$	$171 \pm 2$
$P_1$	15.75	196.36	$14.6 \pm 0.1$	$196.9 \pm 0.4$	$5.3 \pm 0.1$	$209 \pm 1$	$8 \pm 1$	$194 \pm 8$
$Q_1$	7.82	174.07	$7.4 \pm 0.1$	$171.3 \pm 0.9$	$2.6 \pm 0.1$	$185 \pm 2$	$5.3 \pm 0.9$	$190 \pm 10$
$S_2$	14.47	159.92	$14.4 \pm 0.1$	$165.3 \pm 0.6$	$4.93 \pm 0.07$	$172.3 \pm 0.8$	$12.2 \pm 0.7$	$161 \pm 3$
$N_2$	13.97	125.67	$12.7 \pm 0.2$	$127.6 \pm 0.6$	$4.77 \pm 0.06$	$140.2 \pm 0.8$	$11.2 \pm 0.8$	$135 \pm 3$
$M_2$	12.56	220.25	$12.1 \pm 0.1$	$221.9 \pm 0.7$	$3.37 \pm 0.06$	$233 \pm 1$	$6.2 \pm 0.6$	$209 \pm 7$
$K_2$	6.26	174.57	$5.1 \pm 0.1$	$163 \pm 2$	$1.92 \pm 0.07$	$178 \pm 2$	$4.3 \pm 0.5^a$	$164 \pm 3^a$
$MO_3$			$1.1 \pm 0.3$	$155 \pm 17$	$0.5 \pm 0.1$	$153 \pm 14$	$0.4 \pm 0.6^b$	$276 \pm 94^b$
$MK_3$			$1.0 \pm 0.3$	$222 \pm 18$	$0.3 \pm 0.1$	$182 \pm 27$	$0.3 \pm 0.5^b$	$257 \pm 123^b$
$SK_3$			$0.3 \pm 0.3$	$325 \pm 7$	$0.1 \pm 0.1$	$343 \pm 5$	$0.5 \pm 0.6$	$348 \pm 134$
$M_4$			$0.90 \pm 0.05$	$152 \pm 4$	$0.23 \pm 0.05$	$158 \pm 12$	$0.8 \pm 0.4$	$144 \pm 28$
$MS_4$			$0.70 \pm 0.06$	$192 \pm 5$	$0.30 \pm 0.04$	$187 \pm 8$	$0.8 \pm 0.4$	$185 \pm 33$
$S_4$			$0.13 \pm 0.06$	$312 \pm 26$	$0.4 \pm 0.4$	$286 \pm 67$	$0.5 \pm 0.4$	$76 \pm 57$

Note. Both amplitude in centimeters (A) and phase in degrees ( $\phi$ ) are shown as mean  $\pm$  2 S.D. The precision of the mean reflects the highest place value of 2 S.D. In the ocean pressure record,  $SO_3$  cannot be separated from  $MK_3$  and an inference method is not used.

<sup>a</sup>Solutions derived using an inference method. <sup>b</sup>Solutions that do not meet a signal-to-noise ratio of 2.

of pressure data as the diurnal ocean pressure did not show a response to atmospherically driven diurnal temperature fluctuations (section 2.1).

We characterized each tidal record by the percentage of the total variance of the linearly detrended signal that is explained by a tidal tide series recreated from all constituents that have a signal-to-noise ratio exceeding two (Codiga, 2011). We also calculated the percent of total potential energy that each constituent contributes to the tide solution (Codiga, 2011):

$$PE_k = 100 \frac{A_k}{\sum_{i=1}^n A_i} \quad (2)$$

where  $A_k$  is the amplitude of constituent  $k$  and the summation is taken over all constituents included in the solution.

#### 2.4. Removing the IBE

After processing, we corrected for the IBE following Padman, King, et al. (2003). The IBE is the change in sea surface height or, in this case, ice shelf height in response to atmospheric pressure variations. To remove the IBE from GPS elevation records, we observationally constrained the relationship between atmospheric pressure and ice shelf vertical motion at each site, yielding IBE correction factors in units of  $\text{cm hPa}^{-1}$ . We used the atmospheric pressure record from the automatic weather station Sabrina as an approximation of the atmospheric pressure at GZ16 and GZ19. This approach is justified since the atmospheric pressure signal has coherence length scales of hundreds of kilometers.

To evaluate IBE correction factors, we detided the GPS records of vertical motion using the tidal analysis process described in section 2.3. We then applied a low-pass filter with a cutoff of 2 days to both GPS and atmospheric pressure data. This filter approximates the frequency dependence of the IBE (see Padman, King, et al., 2003, for more details). The best fit IBE correction factor at the freely floating site, GZ16, is  $-1.11 \text{ cm hPa}^{-1}$ , which is about 10% larger than the ideal IBE response (Padman, King, et al., 2003). The best fit IBE correction factor at the grounding zone site, GZ19, is  $-0.61 \text{ cm hPa}^{-1}$ , this smaller value being consistent with flexural dampening. We applied these correction factors to the GPS data using the filtered atmospheric pressure record. The mean absolute IBE correction was 10 cm for GZ16 and 5 cm for GZ19.

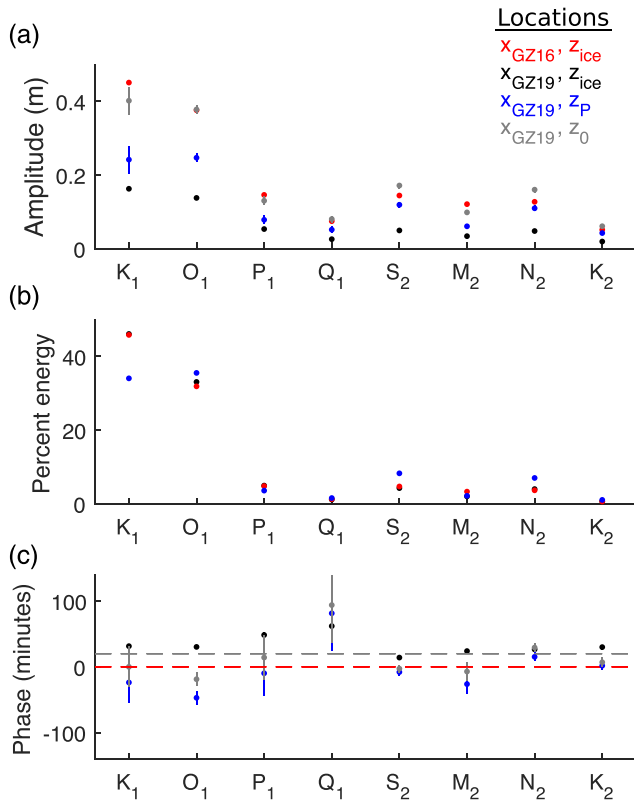


**Figure 3.** Tidal constituent analysis for the eight largest-amplitude tidal constituents. Data are colored by the location of the tide signal: GZ16 GPS station (red), GZ19 GPS station (black), ocean pressure at the sensor at GZ19 (blue), and ocean pressure at the seafloor at GZ19 (gray). Error bars represent the 95% confidence interval. (a) Constituent amplitudes. Ocean pressure amplitude is converted to sea surface height. (b) Percent potential energy contained in each constituent as defined by equation (2). (c) Phase offset with respect to ice shelf deflections at the freely floating site (GZ16). Red dashed line in (c) marks the baseline phase set by GZ16. Gray dashed line marks the expected phase offset for ocean pressure at  $(x_{GZ19}, z_0)$  given tidal wave propagation in shallow water.

We then recomputed tidal constituents (section 2.3) using the IBE-corrected data. This IBE correction did not significantly alter the UTide solutions at either GPS site.

### 2.5. Inferring Ocean Pressure Variations at the Seafloor

To compare these observational data sets, we converted the amplitude of each tidal constituent from units of distance in vertical ice deflection to units of ocean pressure at the seafloor (denoted  $z_0$ ). Since GPS station GZ16 was well outside the limits of ice flexure, we assume that it was in hydrostatic equilibrium with the tide. The time-varying component of ocean pressure at tidal frequency  $\omega_k$  at  $x_{GZ16}$  at depth  $z_0$  was, therefore,

$$P_k(x_{GZ16}, z_0, t) = \rho_w g A_k(x_{GZ16}, z_{ice}) \cos(\omega_k t - \phi_k(x_{GZ16}, z_{ice})) \quad (3)$$

where  $\rho_w$  is the depth-averaged in situ seawater density of  $1,031 \text{ kg m}^{-3}$  (Begeman et al., 2018) and  $A_k(x_{GZ16}, z_{ice})$  is the amplitude of vertical tidal motion of the ice surface, equivalent to the change in ocean cavity thickness assuming constant ice thickness. The phase of the vertical tidal motion of the ice shelf is  $\phi_k(x_{GZ16}, z_{ice})$ . Observations and analysis presented in section 4.5 support the assumption that ice thickness does not vary significantly at tidal frequencies.

At the grounding zone GPS Station GZ19, the ocean pressure at  $z_0$  is the sum of the ocean pressure amplitude at the sensor, which was at fixed distance from the ice surface, and the ocean pressure due to the change in distance between sensor depth  $z_p$  and the seafloor  $z_0$ ,

$$P_k(x_{GZ19}, z_0, t) = P_k(x_{GZ19}, z_p) \cos(\omega_k t - \phi_k(x_{GZ19}, z_p)) + \rho_w g A_k(x_{GZ19}, z_{ice}) \cos(\omega_k t - \phi_k(x_{GZ19}, z_{ice})), \quad (4)$$

where  $P_k(x_{GZ19}, z_p)$  is the tidal pressure amplitude measured at the sensor. The ice shelf is in hydrostatic equilibrium if  $P_k(x, z_p) = 0$ ; thus, the pressure sensor recorded the pressure variations out of local hydrostatic equilibrium.  $A_k(x_{GZ19}, z_{ice})$  is the amplitude of vertical motion of the ice surface. Again, this equation assumes constant ice thickness at tidal frequencies. The phase of the vertical tidal motion of the ice shelf is  $\phi_k(x_{GZ19}, z_{ice})$  and the phase of ocean pressure at the sensor is  $\phi_k(x_{GZ19}, z_p)$ . The second term on the right-hand side can be thought of as a correction for movement of the sensor with the tide as the ice shelf

moved rather than being moored at a fixed distance above the seafloor. We determined the amplitude and phase of ocean pressure constituents at  $(x_{GZ19}, z_0)$  by applying the UTide algorithm to a reconstructed ocean pressure time series following equation (4) and covering the ocean pressure sensor analysis period.

## 3. Results

### 3.1. Tidal Response of the Ice Shelf

Our observations of ice shelf deflections reflected the predominately diurnal tidal forcing in the Ross Sea: the form factor,  $((A_{K_1} + A_{O_1}) / (A_{M_2} + A_{S_2}))$ , comparing diurnal to semidiurnal tides, is about 3 (Table 1 and Figure 3a). The tide height amplitudes at the freely floating site (GZ16) were close to those from the barotropic inverse tide model for the Southern Ocean, CATS2008 (an update to the model described by Padman et al., 2002) (Table 1). Differences in tidal amplitude between ice shelf height and CATS2008 were less than 2 cm for each of the eight major tide constituents.

As expected, vertical tidal deflections of the ice shelf were smaller at the grounding zone site (GZ19) than at the freely floating site (GZ16). The amplitudes of the eight major tide height constituents at GZ19 were 28–38% lower than their respective amplitudes at GZ16 (Table 1 and Figure 3a). The tidal deflection at the grounding zone site also lagged the freely floating site by 20–50 min for major diurnal and semidiurnal constituents (Figure 3c, black points). The phase lag was greater for diurnal constituents than semidiurnal constituents, indicating a frequency-dependent response. The tide model CATS2008 is not likely to have



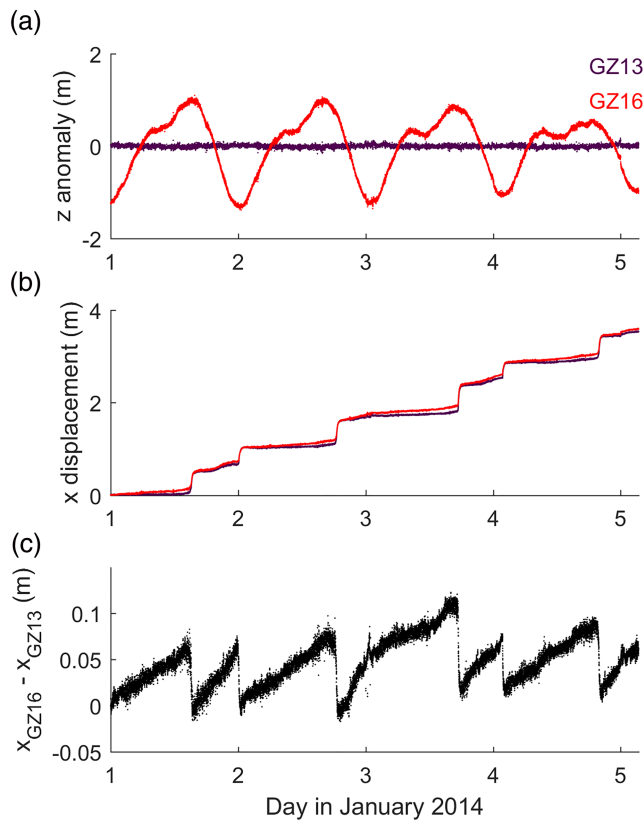


**Figure 4.** Horizontal strain across the grounding zone at tidal frequencies. (a) Tidal height anomaly at freely floating GPS station GZ16 and grounded GPS station GZ13, defined by the difference between instantaneous ice elevation and time-averaged ice elevation. (b) Horizontal ice motion, characterized by bursts of motion during slip events, at GZ13 and GZ16 referenced to their initial positions on 1 January 2014. (c) Distance between GZ13 and GZ16 where the initial distance between the two stations on 1 January 2014 has been subtracted. Horizontal strain is accumulated between slip events and released during slip events.

accurately determined the amplitude of phase of tides near the grounding line; it assumes that the ice is hydrostatic all the way to the grounding line and has a minimum water column thickness of 100 m, even at the grounding line. Thus, CATS2008 may overestimate both tidal amplitudes and tidal wave phase speeds in the grounding zone.

Horizontal ice motion in the grounding zone, as measured by GPS stations, was dominated by the stick-slip cycle of Whillans Ice Stream (Figure 4b; Siegfried et al., 2016; Winberry et al., 2014) (Figure 4). There was also a smaller contribution to horizontal tidal motion of the ice shelf from elastic strain between slip events. Between slip events, that is, on semidiurnal to diurnal timescales, the distance between grounded and fully floating ice ( $x_{GZ16} - x_{GZ13}$ ) of 25 km increased by up to 0.15 m (Figure 4c). Since most of this strain was recovered during slip events, we infer that the strain was predominantly elastic and coincides with ice shelf thinning (stretching). We discuss the magnitude of inferred ice shelf thickness changes due to elastic strain in section 4.5.

Several nonlinear tide constituents,  $MO_3$ ,  $MK_3$ ,  $SK_3$ ,  $M_4$ ,  $MS_4$ , and  $S_4$ , were detectable in ice shelf vertical deflections at both GPS sites on the ice shelf (i.e., their signal-to-noise ratios in UTide exceeded our threshold of 2). The amplitudes of vertical deflections of these components were 0.7–1.1 cm (Table 1). Each of these constituents increased in amplitude from the grounding zone (GZ19) to the freely floating ice shelf (GZ16) (Table 1 and Figure 5b).  $MO_3$  and  $MS_4$  also had a strong expression in horizontal ice velocity consistent with tidal strain softening seen on other ice shelves (Rosier & Gudmundsson, 2018) (Figure 5a). In contrast,  $SK_3$  was enhanced in ice shelf vertical motion relative to its ice velocity expression as seen in the periodogram (Figure 5) but not well determined by the UTide solution (Table 1). The power shown at  $SK_3$  may also include power at  $SP_3$ , as we have less than the full year of data needed to adequately distinguish between these two frequencies. We discuss shallow-water processes for transferring tidal energy to  $SK_3$  in section 4.4.

### 3.2. Tidal Variations in Grounding Zone Ocean Pressure

In hydrostatic equilibrium, the pressure at the ice shelf base is fixed at the glaciostatic pressure, equal to the weight of the ice above (equation (3)).

A pressure sensor mounted to an ice shelf floating in hydrostatic equilibrium would not record any pressure change other those produced by ice shelf mass changes and the IBE. The pressure sensor experienced a long-term linear trend of  $-0.1 \text{ dbar yr}^{-1}$ , which is consistent with the observed basal melting of  $7 \pm 2 \text{ cm yr}^{-1}$  during January 2015 (mean  $\pm 1 \text{ S.D.}$ ), producing a trend of  $-0.06 \pm 0.02 \text{ dbar yr}^{-1}$ , plus a small degree of long-term strain thinning as measured with phase-sensitive radar (Begeman et al., 2018). The ocean pressure in the grounding zone, measured at fixed distance from the ice base, varied by up to  $\sim 1 \text{ dbar}$  over a predominantly diurnal tidal cycle (Figure 2f). Given constant seawater density, we infer that the pressure at the ice base varied by the same amount, exceeding glaciostatic pressure at high tide and falling below glaciostatic pressure at low tide. These ocean pressure variations at the moored sensor indicate that the grounding zone ice was not in hydrostatic equilibrium.

The inferred tidal ocean pressure variations at the seafloor in the grounding zone, described by equation (4), were within tenths of a decibar of the tidal ocean pressure variations inferred outside the grounding zone at GZ16 for most major constituents (cf.  $A_k(x_{GZ19}, z_0)$ , gray points, and  $A_k(x_{GZ16}, z_0)$ , red points, in Figure 3a). Thus, tidal pressure variations were fully transmitted through the grounding zone. The  $K_1$  constituent amplitude is a notable exception; it was  $4.7 \pm 1.8 \text{ cm}$  (mean  $\pm 1 \text{ S.D.}$ ) smaller at the grounding zone site than at the freely floating site ( $A_{K_1}(x_{GZ19}, z_0) < A_{K_1}(x_{GZ16}, z_0)$ , Figure 3a). This 10% difference in amplitude is much larger than typical spatial variability in  $K_1$  over a distance of less than 20 km (on the order of millimeters, Padman, King, et al., 2003).

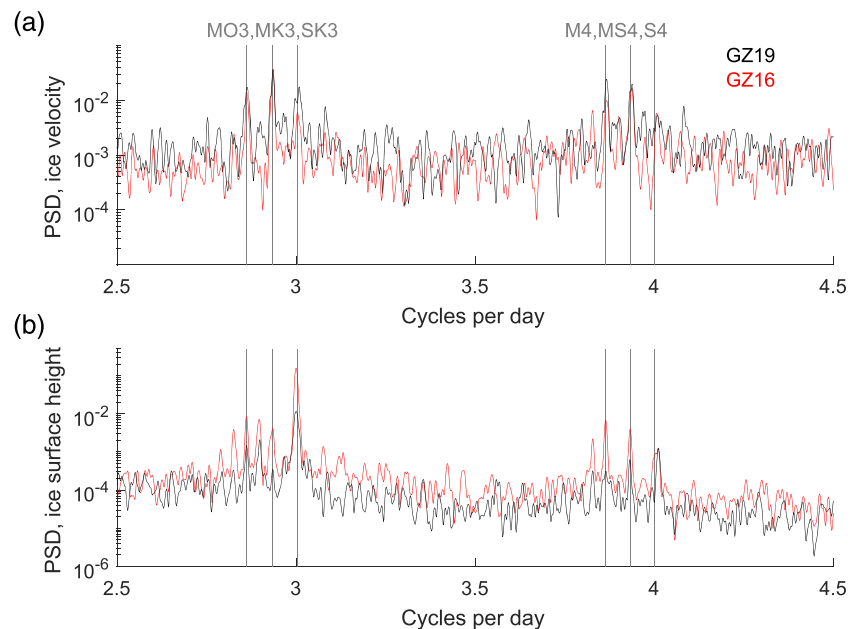


**Figure 5.** Power of Lomb-Scargle spectra of (a) GPS horizontal velocity (GZ16 and GZ19) and (b) GPS elevation (GZ16 and GZ19). Tidal frequencies are indicated (gray vertical lines). Tidal harmonics with three and four cycles per day are shown with vertical lines.

The potential energy loss at  $K_1$  was manifested in ocean pressure; ice shelf vertical deflections had a consistent percent potential energy at  $K_1$ ,  $49.8 \pm 0.1\%$  and  $49.8 \pm 0.3\%$ , while ocean pressure at the moored sensor had only  $34 \pm 5\%$  at  $K_1$  (Figure 3b). No other constituent had as large a difference in potential energy (typically  $<4\%$  difference between ocean pressure and GPS records). By comparing synthetic 54-day ocean pressure records generated from the UTide solution at GZ19, we find that the skipped diurnal measurement for data transmission can only explain a potential energy loss of  $0.05\%$  at  $K_1$ .

Ocean pressure measured at the moored sensor preceded the ice shelf flexural response in the grounding zone (blue points and black points, respectively, Figure 3c). Phase differences between the ice shelf surface elevation response and the ocean pressure response at the seafloor vary from 17 to 49 min. The phase lag at  $Q_1$  ( $94 \pm 57$  min) was anomalously large but is also associated with large error bars that may bring it into closer agreement with other constituents.

The ocean pressure record has a higher noise level and lower precision than the GPS records. Consequently, the percent of temporal variability that is associated with tidal frequencies (i.e., the tidal variance) is lower for the pressure record (47%) compared with the GPS records (93% and 88% for GZ16 and GZ19, respectively). Most ocean pressure constituents identified in the GPS records meet the signal-to-noise ratio criterion of 2, except  $MO_3$  and  $MK_3$  (0.4- and 0.3-cm amplitude, respectively). However, this higher noise level prevents the reliable identification of tidal constituents with higher frequencies than the semidiurnal tides in the ocean pressure record.

### 3.3. Validation of Tidal Ocean Pressure Variations

The amplitude of tidal pressure variations in the grounding zone was independently confirmed using IPSIE (section 2.1), which measured pressure as it traversed the water column vertically several times (Figure 6a). During a single traverse the ocean pressure recorded by IPSIE was well described by equation (1), which assumes constant seawater density. We infer that small discontinuities in pressure ( $<0.1$  dbar) near the observed ice shelf ocean boundary layer were due to a change in seawater density with depth (Begeman et al., 2018). Over the 14 hr of IPSIE deployment the tidal ice shelf deflection ( $\Delta z_{ice, GZ19}$ ) varied by 0.5 m while the ocean pressure at constant distance from the seafloor ( $p_0$ , equation (1)) varied by 1.4 dbar (Figure 6b). Of this pressure difference, 0.5 dbar can be explained by the change in water column height due to ice shelf vertical motions. The remaining 0.9 dbar pressure change is characterized as tidal overpressure as it was in excess of the pressure change in local hydrostatic equilibrium.

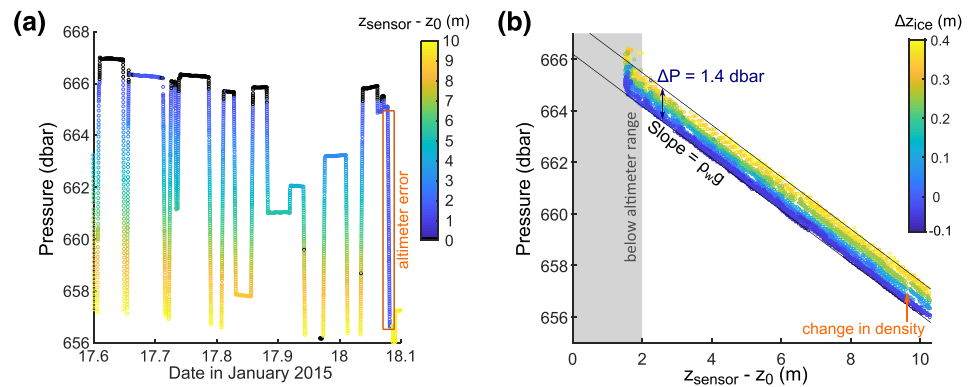


**Figure 6.** Validation of tidal ocean pressure variations. (a) Time series of ocean pressure recorded by IPSIE. Points are colored by the altimeter-determined height above the seafloor. A period of error in the altimeter reading can be seen during the final ascent from the ocean cavity where distance above the seafloor remains small until the instrument is at the top of the ocean cavity. (b) Pressure recorded by IPSIE as a function of sensor distance from the seafloor. Points are colored by the ice shelf deflection at the time of measurement (GZ19). Data points below the altimeter range are located in the shaded region. IPSIE = Instrumentation Package for Sub-Ice Exploration.

We could not compare the ocean pressure data set from IPSIE with that of the moored sensor directly since they were not deployed in overlapping time periods nor could we compare these data sets by tidal constituent since the IPSIE data set was too short. Instead, we compared the ratio of ocean pressure amplitude (in m-hydrostatic-equivalent) to ice shelf deflection amplitude (in meters) between the two data sets. This ratio is 1 when an ice shelf is in hydrostatic equilibrium. The ratio for the IPSIE data set was 2.8. This is broadly consistent with the longer-term relationship between ocean pressure as recorded by the moored sensor and local ice shelf deflections. The ratios for individual constituent amplitudes ranged from 2.5 to 3.5 ( $A_k(x_{GZ19}, z_0)/A_k(x_{GZ19}, z_{ice})$ , Table 1 and equation (4)); the largest-amplitude constituents  $K_1$  and  $O_1$  have ratios 2.5 and 2.8, respectively. The length of the IPSIE data set does not allow us to validate phase differences between ocean pressure determined by the moored sensor and ice shelf vertical deflection.

## 4. Discussion

### 4.1. Tidal Propagation in the Grounding Zone

Our measurements demonstrate that the tidal pressure signal in the grounding zone ocean is of the same magnitude as the signal that would be predicted with a hydrostatic ice shelf. Ice shelf flexure had negligible influence on the tidal variability in ocean pressure in the grounding zone even though flexure greatly reduced ice shelf tidal motion. Flexure likely does play a role in maintaining the force balance at the grounding zone ice-ocean interface. Longitudinal bending stresses or bridging stresses, by which the unsupported weight is transferred laterally via shear stress gradients (van der Veen, 2016), may provide a downward force at high tide and upward force at low tide that opposes the ocean pressure anomaly from glaciostatic pressure at the ice base (Rosier & Gudmundsson, 2018).

The propagation of ocean tidal energy across the grounding zone appears to be consistent with propagation of a shallow-water tidal wave in the absence of ice mechanics. The maximum propagation time of a shallow-water wave is given by a propagation path in a straight line between the freely floating site GZ16 and the grounding zone site GZ19, a distance of 17 km (along the  $x$  axis in Figure 1). This maximum propagation time is given by integrating the shallow water wave speed of  $\sqrt{gH}$  along this path, where the water column thickness  $H$  linearly increases from 10 m at GZ19 to  $30 \pm 5$  m at GZ16 (Horgan et al., 2013). This yields wave speeds from 10 to 17 m/s and a total propagation time of  $20 \pm 1$  min (Figure 3c, gray dashed line). Tide propagation oblique to this axis will result in shorter propagation times; for instance, a wave traveling perpendicular to this axis in constant water depth would reach both sites at the same time. Thus, 20 min is an upper bound on the propagation time between the two sites.

Phase lags in ocean bottom pressure between GZ16 and GZ19 were less than or equal to the maximum propagation time of a shallow-water wave for most of the major diurnal and semidiurnal constituents (cf. gray dots and gray dashed line, Figure 3c). Some of these constituents have the same phase at GZ16 and GZ19, suggesting tidal propagation perpendicular to the axis of flexure, parallel to the coastline. The variability

in phase is erratic and does not show clear patterns with frequency. Diurnal constituents  $K_1$  and  $O_1$  and semidiurnal constituents  $S_2$ ,  $M_2$ , and  $K_2$  show roughly no phase lag, while  $P_1$ ,  $Q_1$ , and  $N_2$  show roughly a 20-min phase lag. Mismatches between the phase predicted by shallow-water wave propagation and the observed ocean pressure phase may be due not only to differences in the orientation of tide propagation but also to uncertainties in the three-dimensional cavity geometry and drag against the seafloor and ice base.

Given that tidal propagation in the grounding zone ocean cavity is broadly consistent with shallow-water wave propagation, we expect that horizontal pressure gradients in the grounding zone due to tides will be similar to pressure gradients predicted by tide models that neglect flexural effects but have realistic representations of water column thickness near the grounding line. Representing ice shelf flexure may become more important when the ratio of the tidal change in water column thickness to the total water column thickness is sufficiently large (Pedley et al., 1986); at a ratio of 1:10 these shallow-water effects did not appear to be important for diurnal and semidiurnal tide modeling. However, shallow-water effects may be scientifically important for other reasons, discussed in section 4.4.

If ice mechanics played no role in the ice shelf's response to tides, then ocean pressure and ice shelf height at GZ19 would be in phase everywhere (i.e., blue, gray, and black points in Figure 3c would align). Our data are consistent with the ice shelf height response in the grounding zone lagging the tidal ocean pressure forcing by tens of minutes. When ocean pressure at a constant geopotential surface ( $P_{z_0}$ ) is decomposed into a nonhydrostatic component (measured at the ice-moored sensor) and the hydrostatic component (measured by the ice surface GPS) per equation (4), the former has a negative phase lag and the latter has a positive phase lag with respect to the phase of  $P_{z_0}$ . Flexural phase lags observed by GPS stations at the grounding zone ice surface are larger than predicted by shallow-water tide propagation (i.e., black points lie above the gray dashed line in Figure 3c). Furthermore, the flexural phase lags were larger than could be produced by a delayed elastic (i.e., primary creep) response alone, which may contribute a phase lag of a few minutes given commonly used rheological parameters (Gudmundsson, 2011). Observed phase lags suggest a viscous response at semidiurnal and diurnal frequencies. Phase lags were larger for diurnal tide frequencies than semidiurnal tide frequencies, consistent with an enhanced viscous response at longer periods (Gudmundsson, 2007, 2011).

Ice shelf flexure in grounding line embayments has an enhanced viscous response to tides relative to straight grounding lines and grounding line promontories (Rabus & Lang, 2002; Wild et al., 2018). The instrumented grounding zone may have a greater flexural phase lag due to its location in a grounding line embayment than nearby grounding zones with a less concave grounding line curvature. This effect of grounding line geometry on ice shelf flexure may explain the smaller phase lags across the grounding zone at a nearby grounding line promontory compared to our site (Siegfried, 2015). In addition to grounding line geometry, this phase lag may be reduced in other grounding zones where the ice is colder or the tidal amplitudes are lower (Reeh et al., 2003). Longer records, collected across a range of grounding line geometries, would help constrain the role of viscous deformation in generating the observed phase lags.

Since the tidal propagation of ocean pressure appears to be unaltered through the grounding zone, the principal effect of ice mechanics on tidal currents in the grounding zone may be through the reduced range of water column height for currents to flow in a 5% change in water column height (in this location, a 0.5 m tidal amplitude in 10 m of water) could produce a ~5% change in current speed, with a smaller change in tidal wave phase speed. This has been the assumption of ocean models of the grounding zone to date, in which the only tidal forcing is the motion of the ice shelf, which pumps water into and out of the expanding and contracting ocean cavity. This volumetric tidal forcing is itself a recent model development (Holland, 2008; Yeager, 2018). However, the hypothesis that volumetric tidal forcing dominates the fluid dynamics has yet to be tested with an ocean model that includes tidal forcing via a propagating tidal pressure wave and a lagged ice shelf response.

#### 4.2. Effects of Tidal Pressure in Excess of Glaciostatic Pressure

Our observations support the use of hydrostatic, tidally varying ocean pressure as the boundary condition for ice sheet and hydrological models at the grounding line where the seafloor, ocean, and ice meet. This has potential application to ice flexure and grounding line migration models, subglacial hydrological models, and basal crevasse models. Hydrostatic, tidally varying ocean pressure at the grounding line has been implemented before in idealized subglacial hydrological models with ice shelf flexure on either side of the grounding line (Rosier & Gudmundsson, 2016; Sayag & Worster, 2013; Thompson et al., 2014).

In this section, we discuss these idealized studies in the context of the local hydrologic setting. Throughout the grounding zone, the ocean pressure at the ice base also varies tidally: from the full hydrostatic tidal pressure range at the grounding line to zero tidal pressure variation at the downstream edge of the grounding zone where the ice shelf is in hydrostatic equilibrium. These basal pressure perturbations in the grounding zone have not been considered in the context of basal crevasse propagation. We present a simple estimate of the tidal pressure contribution to crevasse propagation as a motivation for further study.

At this site, tidal overpressures may induce seawater flow upstream of the grounding line. Hydropotential gradients here are low, leading some to describe this region as an estuary (Carter & Fricker, 2012; Horgan et al., 2013). Radar data consistent with brackish water several kilometers upstream of the grounding line may constitute evidence for hydrologic exchange across the grounding line (Christianson et al., 2013; MacGregor et al., 2011). The extent of inferred brackish water exceeds grounding line migration on tidal timescales (Siegfried, 2015). We hypothesize that the mechanism for transporting salt upstream of the grounding line is ongoing, periodic tidal overpressure, rather than relict salt from a past grounding line inland of the present grounding line.

How tides perturb subglacial hydropotential gradients is highly uncertain due to uncertainty about the bed character (elastic, plastic, viscous, or rigid till) and grounding line position (fixed or migrating) (Rosier & Gudmundsson, 2016; Sayag & Worster, 2011, 2013; Thompson et al., 2014; Walker et al., 2013). For example, subglacial water pressure perturbations from a flexural bulge upstream of the grounding line are the same sign as ocean pressure perturbations and of similar order (tens of kilopascals) when the grounding line is modeled as fixed, enhancing hydrologic exchange across the grounding zone (Walker et al., 2013). However, when the grounding line is allowed to migrate, a hydrological barrier may form due to ice flexure that would prevent this exchange (Sayag & Worster, 2013). Further work on the nature of this transition can be motivated by the possible effects of seawater incursions on grounding line stability. Heat and salt transport associated with seawater flow upstream could raise basal melt rates near the grounding line, as suggested by Parizek et al. (2013) and Milillo et al. (2017).

Ocean pressure is also an important boundary condition for models of basal crevasse propagation. Where ice is in hydrostatic equilibrium, ocean pressure is equal to the glaciostatic pressure at the base of the crevasse. However, in this grounding zone, ocean pressure during high tide exceeds glaciostatic pressure, increasing across the grounding zone as the tidal ice shelf deflection decreases, to a maximum overpressure of  $\sim 10$  kPa at the grounding line (corresponding to about 1 m of tidal height change of freely floating ice). This assumes that the magnitude of tidal ocean pressure variations remains constant from the drill site to the grounding line. At high tides, the overpressure amplitude offsets glaciostatic pressures throughout the crevasse (van der Veen, 1998).

Given the observed overpressure, we estimate its contribution to crevasse propagation using a simple model based on Linear Elastic Fracture Mechanics approach of van der Veen (1998). This model is applicable for stress regimes characterized by uniaxial extension and for a single crevasse propagating up to half the ice thickness (Jimenez & Duddu, 2018); at this site crevasses visible in ice-penetrating radar data are relatively sparse and  $< 50$  m high (Christianson et al., 2016; Jezek & Bentley, 1983). We assume that the stress field in basal ice is well approximated by uniaxial extension in the  $x$  direction and confinement in the  $y$  direction.

We use Glen's flow law to infer longitudinal stress from the longitudinal strain rate

$$\dot{\epsilon}_{xx} = \frac{1}{2} A \tau_{xx}^n \quad (5)$$

with  $A = 2.5 \times 10^{-25} \text{ s}^{-1} \text{ Pa}^{-3}$  and flow exponent  $n = 3$  (Cuffey & Paterson, 2010). The long-term strain rate  $\dot{\epsilon}_{xx}$ , measured from the relative motion of GPS stations on either side of the grounding zone (GZ13 and GZ16), is  $10^{-10} \text{ s}^{-1}$ , consistent with the local synthetic aperture radar interferometry-derived strain rate (Rignot et al., 2011). The long-term strain rate yields a stress estimate of about 80 kPa. We add to this extensional stress the local extensional stress induced by the steady-state curvature of the ice at the grounding zone site (GZ19), as in Logan et al. (2013). This local extensional stress is estimated at 30 kPa using a radius of curvature from kinematic GPS profiles across the flexure zone (Siegfried, 2015). In this stress regime and for critical stress intensity factors from 0.1 to 0.4  $\text{MPa m}^{1/2}$ , a measure of ice toughness (van der Veen, 1998), the maximum diurnal tidal overpressure of 10 kPa increases crevasse height by 7 m at the grounding line.



Tidal overpressure could explain at least 15% of the  $\leq 50$ -m crevasse heights here. Although there is also symmetric tidal underpressure, we expect that the net effect of tides is crevasse propagation as brittle fracture proceeds more rapidly than ductile healing or freezing (Albrecht & Levermann, 2014). Beyond the grounding zone, basal crevasses may creep toward a new equilibrium based on a stress state without overpressure and reduced tidal flexural stresses. Although this tidally driven increase in crevasse height may be limited to the grounding zone, it might be important to account for in models used to infer ice rheology from grounding zone flexure, as crevasses modify the bulk rheology of ice (e.g., reduce the effective Young's modulus) and reduce the width of the grounding zone (Hulbe et al., 2016; Rosier et al., 2017). The additional crevasse area made available by ocean overpressure may modify basal melt rates and associated heat and salt fluxes through the ice shelf ocean boundary layer (Khazendar & Jenkins, 2003; Luckman et al., 2012). Further work is needed to determine whether crevasses significantly influence sub-ice shelf water masses and basal melt rates.

The stress field in the grounding zone is likely more complex than represented here. At this embayment, the ice curvature is most favorable for crevasse propagation (concave upward) at the grounding line and 2–5 km from the grounding line, and tidal flexure also perturbs this curvature (Siegfried, 2015). The phase lag between local ocean pressure and ice shelf flexure, spanning 10–48 min for the major constituents, has potential implications for the force balance in the grounding zone. Where the tidal ocean pressure at the ice base is unequal to the glaciostatic pressure at the ice base, longitudinal bending stresses or bridging stresses may develop and restore force balance (Rosier & Gudmundsson, 2018). These repeated tidal perturbations to the stress field in ice are potentially important for crevasse development as they can change ice rheology (Hughes, 1983). We recommend further investigation of the grounding zone stress field using three-dimensional full Stokes models (e.g., Rosier et al., 2014).

#### 4.3. Possible Explanations for Loss of Ocean Pressure at $K_1$

The only tidal constituent showing a statistically significant loss of tidal potential energy in the grounding zone relative to offshore is  $K_1$ . We seek to explain this observation, keeping in mind two features of the data:

- Feature 1: Tidal potential energy loss favored  $K_1$  over  $O_1$  though these constituents have similar frequencies and amplitudes (Figure 3a).
- Feature 2: Potential energy loss was manifested in the ocean pressure amplitude and not in ice shelf height amplitude (Figure 3b).

We considered the following mechanisms for the loss of tidal potential energy: (i) internal tide generation, (ii) vibrational resonance of the ice shelf, (iii) viscous deformation of ice, (iv) crevassing, (v) current drag, (vi) grounding line migration, and (vii) subglacial hydrologic flow.

(i) *Internal tide generation.* If barotropic energy at  $K_1$  was converted to baroclinic energy (internal tides), ocean pressure amplitudes would be depleted to a greater extent than ice shelf height amplitudes, which are influenced by far-field flexure (e.g., at GZ16). There is an abrupt increase in seafloor depth between the two sites (Horgan et al., 2013) that may excite diurnal topographic vorticity waves (Mueller et al., 2012). These tide-topography interactions may be very sensitive to frequency (e.g., Sun et al., 2019) and thus may explain Feature 1. However, we would expect to detect these vorticity waves as enhanced diurnal currents at our site, which is less than 1 km away from the topography, given that these waves have slow radiation of energy away from the generating topography. There is no evidence for diurnal currents at middepth in the water column (Begeman et al., 2018), though they could be present at other depths (tidal current profiles can be quite depth-dependent as shown by Jenkins, 2016; Makinson, 2002).

(ii) *Vibrational resonance of the ice shelf.* Some lower order vibrational modes of the Ross Ice Shelf could have periods close to 12 hr that may be excited by wave energy or other energetic events (Godin & Zabolin, 2016). Since these vibrations are expected to decrease close to the grounding zone, their magnitude could be greater at freely floating site GZ16 than grounding zone site GZ19. However, the frequency of these vibrational modes is set in part by ice shelf thickness and water column thickness, which vary spatially. Thus, as the ocean and solid Earth waves that excite these vibrations vary in their spatial distribution and propagation paths through the ice shelf, they should generate vibrations that span a range of frequencies. If that lower order vibrational mode has a period close to 12 hr, it likely spans both  $K_1$  and  $O_1$ ; vibrational resonance of the ice shelf is inconsistent with Feature 1.

- (iii) *Viscous deformation of ice.* Viscous deformation of ice is a poor candidate for tidal energy dissipation, as these losses should be seen more strongly in ice shelf deflection than in ocean pressure (inconsistent with Feature 2). Viscous deformation should also deplete similar amounts of energy at similar forcing frequencies (inconsistent with Feature 1).
- (iv) *Crevasse propagation.* Crevasse propagation is likely to dissipate similar amounts of energy at  $O_1$  and  $K_1$  because the magnitude of ice flexure and ocean pressure perturbation, assumed to drive crevasse propagation, was similar at both frequencies (inconsistent with Feature 1). Thus, we exclude crevasse propagation as a candidate for tidal energy dissipation.
- (v) *Current drag.* Tidal energy dissipation by current drag can explain our observations if the spatial change in tidal currents is sufficiently large to differentially affect ocean pressure but not so spatially extensive that it affects the ice flexural response (i.e., to account for Feature 2). Tidal dissipation by current drag may also explain preferential energy losses at  $K_1$  (consistent with Feature 1) if currents at  $K_1$  frequencies were sufficiently stronger than at  $O_1$  frequencies. Since tidal dissipation by drag is proportional to current speed cubed, differences in current magnitude at  $K_1$  and  $O_1$  would be amplified in tidal energy dissipation at  $K_1$  and  $O_1$ . Tidal modeling to evaluate this mechanism is beyond the scope of this study. However, tidal current speeds are likely on the order of a few millimeter per second based on local current observations (Begeman et al., 2018) while local tidal currents from the CATS2008 barotropic model (with a 100-m-thick water column) are about  $10 \text{ mm s}^{-1}$  for  $K_1$  and  $O_1$ . These estimates suggest minimal tidal energy dissipation by current drag.
- (vi) *Grounding line migration.* Tidal grounding line migration may explain the decrease in ocean pressure amplitude by increasing ocean cavity volume but would likely also affect ice shelf height amplitudes (inconsistent with Feature 2). Additionally, grounding line migration is likely to be equally extensive at both  $K_1$  and  $O_1$  frequencies given their similar amplitudes, depleting similar amounts of tidal potential energy. Grounding line migration is inconsistent with Feature 1 and possibly inconsistent with Feature 2.
- (vii) *Subglacial hydrological flow.* Tidal potential energy, manifested alternately as overpressure and underpressure at the grounding line, may be converted first to the kinetic energy of water flow across the grounding line. This energy may then be converted to potential energy as subglacial water flows up hydropotential gradients or it may be frictionally dissipated. As tidal potential energy drives subglacial water flow, the tidal amplitude of ocean pressure should decrease, consistent with Feature 2. One can account for a wide range of tidal energy dissipation values by subglacial water flow depending on the choice of effective hydraulic conductivity, conduit geometry and drag in the subglacial hydrologic system (Werder et al., 2013). During slip events ice and till may be less tightly coupled, enhancing hydraulic conductivities and water flow across the grounding line. Granular till modeling suggests that porosity and thus hydraulic conductivity could increase during slip events (Damsgaard et al., 2016). This hydrological mechanism may also explain preferential dissipation at  $K_1$ . Slip events appear to be set primarily by the diurnal tide, occurring once or twice daily at high tide and low tide (sometimes skipping low tide) (Bindshadler, 2003; Beem et al., 2014; Siegfried et al., 2016). Although  $K_1$  and  $P_1$  cannot be separated in our relatively short ocean pressure record, the GPS height records reveal that they are roughly in phase during the period of our observations. This yields a combined diurnal pressure forcing that is greater during  $K_1$  peaks than at  $O_1$  peaks. Thus, slip events and any associated dissipation may be favored at  $K_1$  rather than  $O_1$  due to short-term synchronicity of  $K_1$  with  $P_1$  (Feature 1). In this study, we did not undertake an analysis of the timing and character of slip events, which would be needed to fully explain the observed frequency-dependent tidal dissipation. However, it is unlikely that the slip events themselves induce barotropic waves sufficient in amplitude to interact significantly with tidal waves. The volumetric change in the ocean cavity from slip events will be small compared with the volumetric change from tides; the vertical displacement during slip events falls below the GPS detection limit of  $\sim 5 \text{ mm}$  (Bindshadler, 2003) while tidal deflections are on the order of tens of centimeters. Grounding line migration during slip events, which could also change ocean cavity volume, will also be small as it would be associated with vertical displacement of the ice, as discussed in (vi).

If the subglacial hydrology mechanism (vi) can be reconciled with observations, the frequency of tidal energy dissipation offers indirect evidence for changes in the subglacial hydrologic system during periods of fast ice flow. This is an alluring possibility for remotely sensed observations of hydrologic change. However, ocean

modeling of  $K_1$  and  $O_1$  with better ocean cavity geometry may reveal preferential energy loss from  $K_1$  due to topographic vorticity wave generation (i) or current drag (iv).

#### 4.4. Using Nonlinear Tides to Study Nonlinearities in the Ice Shelf-Ocean System

Nonlinear tides on ice shelves have the potential to reveal nonlinearities in the ice shelf-ocean system (King et al., 2011; Makinson et al., 2012; Pedley et al., 1986). While it is easier to detect nonlinear tide constituents in ice surface motion than in ocean pressure or currents, tide constituents at the ice surface represent a convolution of nonlinear ocean processes and ice or till deformation (Doake et al., 2002; King et al., 2011; Makinson et al., 2012; Rosier & Gudmundsson, 2016; Pedley et al., 1986; Thomas, 2007). On the other hand, nonlinear tide constituents in ocean pressure are thought to largely represent nonlinear ocean processes (Pedley et al., 1986). Whereas ocean pressure and tidal currents can affect ice shelf motion by imposing body stresses, ice shelf tidal motion is not thought to have a significant effect on ocean pressure through drag or grounding line migration. This is supported by our finding that ocean pressure in the grounding zone is imperceptibly perturbed by ice flexure (i.e., the phase of ocean pressure in the grounding zone is consistent with shallow-water tide propagation).

Due to the level of noise in the pressure record from the sensor deployed in this study, we were unable to reliably determine the amplitude of nonlinear tide constituents in the grounding zone. Future studies could gain insights into nonlinear ice rheology and basal deformation and sliding by improving upon these measurements. A priority for these studies should be increasing the signal-to-noise ratio of ocean pressure observations. Strategies for increasing the signal-to-noise ratio include increasing the amplitude of pressure fluctuations, recording pressure at the seafloor rather than at fixed distance from the ice base, and increasing measurement precision, which was undermined by data transmission limitations in this study. We were also limited by a short (2 months) time series. A longer time series would both improve the signal at tide constituents and allow the separation of more nonlinear (higher frequency) tide constituents.

Despite limitations in our data set, the measurements suggest that shallow-water tide transformations are important in the grounding zone. In particular, nonlinear tide constituents  $SK_3$  and  $SP_3$  appear in vertical ice deflections without a corresponding expression in horizontal ice velocity. This indicates a source in the nonlinear terms of the shallow water equations rather than ice or till deformation, which would induce a horizontal ice velocity expression as well. The decrease in nonlinear tide amplitudes from the freely floating ice shelf to the grounding zone was unexpected; typically nonlinear tides increase in amplitude in shallow water (King et al., 2011). We hypothesize that these nonlinear tide amplitudes do increase with proximity to the grounding zone, a trend that would be detectable with an ocean pressure record of higher quality, and that these nonlinear tides are dampened only in the vertical ice deflection in the grounding zone.

Of the nonlinear shallow water processes, frictional drag between ocean currents and the seafloor or ice base is a likely source for amplifying  $SK_3$ . In the absence of turbulence data or current velocity data, it is difficult to evaluate the magnitude of frictional drag across tide constituents. However, the CATS2008 tide model does predict that  $K_1$  and  $S_2$  are the largest-amplitude diurnal and semidiurnal current velocity constituents, which would yield a stronger  $SK_3$  through current drag. As discussed in section 4.3, preferential dissipation at  $K_1$  may be evidence for current drag. A motivation for improving ocean pressure data is constraining the drag coefficients which describe frictional drag between ocean currents and the ice base or seafloor. Spatial variations in nonlinear tide constituents could offer observational constraints on the effective drag coefficient over larger regions than can be constrained with in situ turbulence packages. These constraints could improve both barotropic tide models and ocean circulation models for which the drag coefficient is a tunable parameter (Gwyther et al., 2015; Padman et al., 2018). These model improvements would benefit ice shelf melt rate predictions, which are determined jointly by ocean currents, their tidal variability, and the ice shelf drag coefficient (Holland & Jenkins, 2001; Jourdain et al., 2019).

#### 4.5. Methodological Uncertainties in Tidal Analyses

The short length of the ocean pressure record necessitated the use of an inference method for several tidal constituents (section 2.3). The inference method used to derive the amplitude and phase of several major tide constituents appears to be robust. The  $P_1:K_1$  amplitude ratio given by the GZ16 tide solution (0.325) is similar to values measured at ocean bottom sensors elsewhere in the world (0.29–0.34) and the value of 0.318 derived from equilibrium tide theory (Ray, 2017). The resulting error in the  $K_1$  ocean pressure amplitude due to inaccuracy in the  $P_1:K_1$  ratio of GZ16 should be on the order of a few mm given the difference between the 2013 ratio and 2012 ratio (0.312) at GZ16 and the ratio at GZ19 (0.326) during 2015. The uncertainty in

the  $K_1$  solution due to measurement noise of 4 cm is much larger than the uncertainty from inference. The  $K_2:S_2$  ratio at GZ16 (0.351) is slightly higher than the  $K_2:S_2$  ratio at GZ19 (0.391). Thus,  $K_2$  amplitudes may have an uncertainty of up to  $\pm 0.5$  cm, so we revise the uncertainty determined by UTide upwards from  $\pm 0.2$  cm (Table 1).

To convert between ice shelf elevation changes and ocean pressure changes (equations (3) and (4)), we assumed that neither ice shelf thickness nor seawater density vary at tidal frequencies. If ice shelf thickness is constant, then the measured change in ice shelf elevation is equal to the change in water column thickness. The agreement between ocean pressure tidal range measured by IPSIE and ocean pressure tidal range inferred using equation (4) supports this assumption. We also validated this assumption by estimating strain thinning across the grounding zone from observations of horizontal strain (Figure 4a). As stated in section 3.1, most of the observed horizontal tidal motion was due to elastic extension and compression. Given  $<0.1$ -m horizontal diurnal deflection per 1-m vertical diurnal tidal deflection (GZ16) and assuming Poisson's ratio was 0.3 (Cuffey & Paterson, 2010), we estimate that the ice thickness changed by at most 2 mm due to elastic compression and extension on diurnal timescales. This is an upper bound on ice thickness changes as some of the horizontal motion may have been due to viscous strain. Consequently, tidal amplitudes may be overestimated by up to about half the tidal thickness change, or 1 mm—an acceptable level of error.

We assumed that seawater density did not vary at tidal frequencies (i.e., that steric effects could be neglected). However, several lines of evidence suggest that seawater densities are relatively constant. Seawater density did not vary significantly over the 14-hr IPSIE deployment (section 3.3) or the three CTD casts collected over one week of borehole measurements (Begeman et al., 2018). Given the 2- to 6-year residence time of waters circulating below Ross Ice Shelf and the great distance of the study site from the ice front (Reddy et al., 2010), seasonal variability should be greatly dampened and water mass properties should have remained roughly constant over the 54-day ocean pressure record. While subglacial discharge events (Fricker & Scambos, 2009; Siegfried et al., 2014) may modify seawater densities (e.g., Washam et al., 2019), meltwater concentrations would need to change substantially to significantly affect ocean pressure. For example, the depth-averaged seawater density would have to decrease by 0.5% to decrease ocean pressure by 0.05 dbar, equivalent to adding 18% meltwater by volume by mixing with the observed water mass (decreasing salinity from 34.8 to 33.4 g kg<sup>-1</sup>) (Begeman et al., 2018). This perturbation is on the order of a subglacial lake drainage event, which happens every few years (Carter & Fricker, 2012; Siegfried & Fricker, 2018). We conclude that steric effects have not significantly altered tidal variations in ocean pressure or ice shelf vertical deflections.

The ocean pressure sensor may have experienced some tidal motion as it hung in the water column. We minimized such motion by reinforcing the sensor cable with a steel cable. Since both IPSIE, for which depth variations are known, and the moored sensor, for which depth variations are assumed equal to the ice surface motion, measure a similar ocean pressure response to tides, we infer that the moored sensor accurately measured the vertical tidal motion of the ice shelf without significant current-induced motion. This is consistent with the low measured current velocities of  $1 \pm 0.3$  cm s<sup>-1</sup> and the lack of detectable tidal variations in current velocities (Begeman et al., 2018).

## 5. Summary and Outlook

We have presented the first concurrent observations of ocean pressure and ice shelf motion in the grounding zone of an Antarctic ice shelf. Tidal ocean pressure variations in the grounding zone, measured over 54 days between January and March 2015, were of the same magnitude as tidal ocean pressure variations just seaward of the grounding zone. These pressure variations preceded ice shelf flexure, which may have implications for tidal currents in the grounding zone. Ocean pressure variations at the grounding line will be transmitted into the subglacial environment, which may affect ice flow and subglacial hydrology. We hypothesize that ocean pressure maxima at high tides inject seawater into the subglacial environment and enhance basal crevassing in grounding zones.

We have recommended several strategies to increase the value of ocean pressure data collected in ice shelf grounding zones, chiefly increasing the resolution of the logged data and obtaining a longer time series. We also propose detailed bathymetric surveys near the grounding line (e.g., active seismic surveys or autonomous underwater vehicle multibeam surveys). With better constraints on water column thickness and local tide records, tide models could be configured to evaluate shallow water effects, particularly the



### Acknowledgments

Our work was supported by the U.S. National Science Foundation, Section for Antarctic Sciences, Antarctic Integrated System Science program as part of the interdisciplinary Whillans Ice Stream Subglacial Access Research Drilling (WISSARD) project. C. B. B. was supported by the National Science Foundation Graduate Research Fellowship and the University of California President's Dissertation Year Fellowship. S. T. was supported by NSF-ANT-0838947. L. P. was supported by NSF-ANT-1443677 and NASA NNX17AG63G. M. K. was supported by the Australian Research Council's Special Research Initiative for Antarctic Gateway Partnership (Project ID SR140300001). M. R. S. was supported by NSF-ANT-083885 and 1543441. University of Nebraska, Lincoln drill team created the borehole for ocean pressure sensor deployment. The U.S. Antarctic Program enabled our fieldwork, and New York Air National Guard and Kenn Borek Air provided air support. Sarah Neuhaus assisted with ocean pressure sensor deployment. Daniel Sampson at UC Santa Cruz designed, engineered, and assembled most of the in situ borehole sensor systems for this project and assisted with data reduction and interpretation. Brecky Morris wrote the code for ocean pressure data collection and satellite transmission, with the help of Campbell Scientific Canada. Hannah Dailey assisted in preliminary tidal analysis. Richard Ray provided useful input on tidal analysis methods. We thank Matt Hoffman for discussions on the feasibility of ocean-subglacial hydrological exchange. This research is based on data services provided by the UNAVCO Facility with support from the National Science Foundation (NSF) and National Aeronautics and Space Administration (NASA) under NSF Cooperative Agreement EAR-0735156. The authors appreciate the support of the University of Wisconsin-Madison Automatic Weather Station Program for the data set, data display, and information, NSF Grant ANT-1543305. The authors declare no competing financial interests. GPS data can be accessed at the UNAVCO data center (<https://www.unavco.org/data/doi/doi:10.7283/T53R0RPD>). Pressure data are available at the National Centers for Environmental Information, Accession Number 0209188.

role of drag and the value of drag coefficients. Future studies could also use a minimum of three sites where ocean pressures and current velocities are measured to provide a local estimate of tidal energy dissipation (Hendershott, 1972). Since this study only offers two sites where tidal amplitudes are constrained and tidal current velocities are unknown, we were unable to provide an estimate of tidal energy dissipation. However, our observations indicate potential energy was lost at  $K_1$ , consistent with hydrologic exchange across the grounding line during the slip events that characterize Whillans Ice Stream flow. Further work is needed to account for tidal energy conservation at other slip event frequencies.

With respect to ice sheet and ocean modeling, our work raises the question of whether it is necessary to capture tide transformations in the grounding zone to accurately simulate sub-ice shelf ocean circulation, subglacial hydrology, and melt rates. We propose further observational campaigns and modeling efforts aimed at addressing the following questions:

1. Are tidal ocean pressure variations in grounding zones consistently equal to hydrostatic ocean pressure variations seaward of the grounding zone, or are they affected by other factors (e.g., grounding line migration, features of the subglacial hydrologic system, or frictional properties of the seafloor and ice shelf base)?
2. Are tidal currents near the grounding line significantly modified by the hinging motion of the ice shelf, which lags tidal pressure gradients?
3. To what degree are basal crevasses propagated by the combination of tidal overpressure and tidal flexure?
4. Does tidal ocean pressure at the grounding line modulate subglacial hydrology and drive seawater incursions upstream of the grounding line?
5. Do these consequences of a nonhydrostatic grounding zone have significant nonlocal effects on ocean circulation and melt rates?

A better understanding of tidal processes near grounding lines is a prerequisite for improvements to ice sheet and ocean models. Outcomes from this study and these additional studies would bring us closer to adequate representations of this dynamically important region.

### References

- Albrecht, T., & Levermann, A. (2014). Fracture-induced softening for large-scale ice dynamics. *The Cryosphere*, 8(2), 587–605. <https://doi.org/10.5194/tc-8-587-2014>
- Anandakrishnan, S., Voigt, D. E., Alley, R. B., & King, M. A. (2003). Ice stream D flow speed is strongly modulated by the tide beneath the Ross Ice Shelf. *Geophysical Research Letters*, 30(7), 1361. <https://doi.org/10.1029/2002GL016329>
- Beem, L. H., Tulaczyk, S. M., King, M. A., Bougamont, M., Fricker, H. A., & Christoffersen, P. (2014). Variable deceleration of Whillans Ice Stream, West Antarctica. *Journal of Geophysical Research: Earth Surface*, 119, 212–224. <https://doi.org/10.1002/2013JF002958>
- Begeman, C. B., Tulaczyk, S. M., Marsh, O. J., Mikucki, J. A., Stanton, T. P., Hodson, T. O., et al. (2018). Ocean stratification and low melt rates at the Ross Ice Shelf grounding zone. *Journal of Geophysical Research: Oceans*, 123, 7438–7452. <https://doi.org/10.1029/2018JC013987>
- Bindschadler, R. A. (2003). Tidally controlled stick-slip discharge of a West Antarctic Ice Stream. *Science*, 301(5636), 1087–1089. <https://doi.org/10.1126/science.1087231>
- Brunt, K. M., Fricker, H. A., & Padman, L. (2011). Analysis of ice plains of the Filchner–Ronne Ice Shelf, Antarctica, using ICESat laser altimetry. *Journal of Glaciology*, 57(205), 965–975. <https://doi.org/10.3189/002214311798043753>
- Brunt, K. M., King, M. A., Fricker, H. A., & MacAyeal, D. R. (2010). Flow of the Ross Ice Shelf, Antarctica, is modulated by the ocean tide. *Journal of Glaciology*, 56(195), 157–161.
- Budd, W. F., Keage, P. L., & Blundy, N. A. (1979). Empirical studies of ice sliding. *Journal of Glaciology*, 23(89), 157–170. <https://doi.org/10.3189/S0022143000029804>
- Carter, S. P., & Fricker, H. A. (2012). The supply of subglacial meltwater to the grounding line of the Siple Coast, West Antarctica. *Annals of Glaciology*, 53(60), 267–280. <https://doi.org/10.3189/2012AoG60A119>
- Chen, G. (1998). GPS kinematic positioning for the airborne laser altimetry at Long Valley, California (Thesis), Massachusetts Institute of Technology. Dept. of Earth, Atmospheric, and Planetary Sciences.
- Christianson, K., Jacobel, R. W., Horgan, H. J., Alley, R. B., Anandakrishnan, S., Holland, D. M., & DallaSanta, K. J. (2016). Basal conditions at the grounding zone of Whillans Ice Stream, West Antarctica, from ice-penetrating radar. *Journal of Geophysical Research: Earth Surface*, 121, 1954–1983. <https://doi.org/10.1002/2015JF003806>
- Christianson, K., Parizek, B. R., Alley, R. B., Horgan, H. J., Jacobel, R. W., Anandakrishnan, S., et al. (2013). Ice sheet grounding zone stabilization due to till compaction. *Geophysical Research Letters*, 40, 5406–5411. <https://doi.org/10.1002/2013GL057447>
- Codiga, D. L. (2011). Unified tidal analysis and prediction using the UTide Matlab functions. Narragansett, RI: Graduate School of Oceanography, University of Rhode Island. <ftp://www.po.gso.uri.edu/pub/downloads/codiga/pubs/2011Codiga-UTide-Report.pdf>
- Cuffey, K., & Paterson, W. S. B. (2010). *The physics of glaciers* (4th ed). Burlington, MA: Butterworth-Heinemann/Elsevier.
- Damsgaard, A., Egholm, D. L., Beem, L. H., Tulaczyk, S., Larsen, N. K., Piotrowski, J. A., & Siegfried, M. R. (2016). Ice flow dynamics forced by water pressure variations in subglacial granular beds. *Geophysical Research Letters*, 43, 12,165–12,173. <https://doi.org/10.1002/2016GL071579>
- Dinniman, M., Asay-Davis, X., Galton-Fenzi, B., Holland, P., Jenkins, A., & Timmermann, R. (2016). Modeling ice shelf/ocean interaction in Antarctica: A review. *Oceanography*, 29(4), 144–153. <https://doi.org/10.5670/oceanog.2016.106>
- Doake, C. S. M., Corr, H. F. J., Nicholls, K. W., Gaffikin, A., Jenkins, A., Bertiger, W. I., & King, M. A. (2002). Tide-induced lateral movement of Brunt Ice Shelf, Antarctica. *Geophysical Research Letters*, 29(8), 1226. <https://doi.org/10.1029/2001GL014606>



- Dupont, T. K., & Alley, R. B. (2005). Assessment of the importance of ice-shelf buttressing to ice-sheet flow. *Geophysical Research Letters*, 32, L04503. <https://doi.org/10.1029/2004GL022024>
- Foreman, M. G. G. (1977). Manual for tidal heights analysis and prediction. *Marine Science Report*, 77(10), 101.
- Foreman, M. G. G. (1978). Manual for tidal currents analysis and prediction. *Marine Science Report*, 78(9), 70.
- Fricker, H. A., & Padman, L. (2006). Ice shelf grounding zone structure from ICESat laser altimetry. *Geophysical Research Letters*, 33, L15502. <https://doi.org/10.1029/2006GL026907>
- Fricker, H. A., & Scambos, T. (2009). Connected subglacial lake activity on lower Mercer and Whillans Ice Streams, West Antarctica, 20032008. *Journal of Glaciology*, 55(190), 303–315.
- Godin, O. A., & Zabolotin, N. A. (2016). Resonance vibrations of the Ross Ice Shelf and observations of persistent atmospheric waves. *Journal of Geophysical Research: Space Physics*, 121, 10,157–10,171. <https://doi.org/10.1002/2016JA023226>
- Goldberg, D. N., Gourmelen, N., Kimura, S., Millan, R., & Snow, K. (2018). How accurately should we model ice shelf melt rates? *Geophysical Research Letters*, 46, 189–199. <https://doi.org/10.1029/2018GL080383>
- Gudmundsson, G. H. (2006). Fortnightly variations in the flow velocity of Rutford Ice Stream, West Antarctica. *Nature*, 444(7122), 1063–1064. <https://doi.org/10.1038/nature05430>
- Gudmundsson, G. H. (2007). Tides and the flow of Rutford Ice Stream, West Antarctica. *Journal of Geophysical Research*, 112, F04007. <https://doi.org/10.1029/2006JF000731>
- Gudmundsson, G. H. (2011). Ice-stream response to ocean tides and the form of the basal sliding law. *The Cryosphere*, 5(1), 259–270. <https://doi.org/10.5194/tc-5-259-2011>
- Gwyther, D. E., Coughon, E. A., Galton-Fenzi, B. K., Roberts, J. L., Hunter, J. R., & Dinniman, M. S. (2016). Modelling the response of ice shelf basal melting to different ocean cavity environmental regimes. *Annals of Glaciology*, 57(73), 131–141. <https://doi.org/10.1017/aog.2016.31>
- Gwyther, D. E., Galton-Fenzi, B. K., Dinniman, M. S., Roberts, J. L., & Hunter, J. R. (2015). The effect of basal friction on melting and freezing in ice shelf-ocean models. *Ocean Modelling*, 95, 38–52. <https://doi.org/10.1016/j.ocemod.2015.09.004>
- Hendershott, M. C. (1972). The effects of solid Earth deformation on global ocean tides. *Geophysical Journal of the Royal Astronomical Society*, 29(4), 389–402. <https://doi.org/10.1111/j.1365-246X.1972.tb06167.x>
- Holland, P. R. (2008). A model of tidally dominated ocean processes near ice shelf grounding lines. *Journal of Geophysical Research*, 113, C11002. <https://doi.org/10.1029/2007JC004576>
- Holland, D. M., & Jenkins, A. (2001). Adaptation of an isopycnic coordinate ocean model for the study of circulation beneath ice shelves. *Monthly Weather Review*, 129(8), 1905–1927. [https://doi.org/10.1175/1520-0493\(2001\)129<1905:AOAICO>2.0.CO;2](https://doi.org/10.1175/1520-0493(2001)129<1905:AOAICO>2.0.CO;2)
- Horgan, H. J., Alley, R. B., Christianson, K., Jacobel, R. W., Anandakrishnan, S., Muto, A., et al. (2013). Estuaries beneath ice sheets. *Geology*, 41, 1159–1162. <https://doi.org/10.1130/G34654.1>
- Horgan, H. J., Christianson, K., Jacobel, R. W., Anandakrishnan, S., & Alley, R. B. (2013). Sediment deposition at the modern grounding zone of Whillans Ice Stream, West Antarctica. *Geophysical Research Letters*, 40, 3934–3939. <https://doi.org/10.1002/grl.50712>
- Hughes, T. (1983). On the disintegration of ice shelves: The role of fracture. *Journal of Glaciology*, 29(101), 98–117. <https://doi.org/10.3189/S0022143000005177>
- Hulbe, C. L., Klinger, M., Masterson, M., Catania, G., Cruikshank, K., & Bugni, A. (2016). Tidal bending and strand cracks at the Kamb Ice Stream grounding line, West Antarctica. *Journal of Glaciology*, 62(235), 816–824. <https://doi.org/10.1017/jog.2016.74>
- Jenkins, A. (2016). A simple model of the ice shelf-ocean boundary layer and current. *Journal of Physical Oceanography*, 46(6), 1785–1803. <https://doi.org/10.1175/JPO-D-15-0194.1>
- Jezek, K. C. (1984). Recent changes in the dynamic condition of the Ross Ice Shelf, Antarctica. *Journal of Geophysical Research*, 89(B1), 409–416.
- Jezek, K. C., & Bentley, C. R. (1983). Field studies of bottom crevasses in the Ross Ice Shelf, Antarctica. *Journal of Glaciology*, 29(101), 118–126. <https://doi.org/10.3189/S0022143000005189>
- Jimenez, S., & Duddu, R. (2018). On the evaluation of the stress intensity factor in calving models using linear elastic fracture mechanics. *Journal of Glaciology*, 64, 759–770. <https://doi.org/10.1017/jog.2018.64>
- Jourdain, N. C., Molines, J.-M., Le Sommer, J., Mathiot, P., Chanut, J., de Lavergne, C., & Madec, G. (2019). Simulating or prescribing the influence of tides on the Amundsen Sea ice shelves. *Ocean Modelling*, 133, 44–55. <https://doi.org/10.1016/j.ocemod.2018.11.001>
- Khazendar, A., & Jenkins, A. (2003). A model of marine ice formation within Antarctic ice shelf rifts. *Journal of Geophysical Research*, 108(C7), 3235. <https://doi.org/10.1029/2002JC001673>
- King, M. A., & Aoki, S. (2003). Tidal observations on floating ice using a single GPS receiver. *Geophysical Research Letters*, 30(3), 1138. <https://doi.org/10.1029/2002GL016182>
- King, M. A., Makinson, K., & Gudmundsson, G. H. (2011). Nonlinear interaction between ocean tides and the Larsen C Ice Shelf system. *Geophysical Research Letters*, 38, L08501. <https://doi.org/10.1029/2011GL046680>
- King, M. A., Murray, T., & Smith, A. M. (2010). Non-linear responses of Rutford Ice Stream, Antarctica, to semi-diurnal and diurnal tidal forcing. *Journal of Glaciology*, 56(195), 167–176. <https://doi.org/10.3189/002214310791190848>
- King, M. A., Padman, L., Nicholls, K., Clarke, P. J., Gudmundsson, G. H., Kulesa, B., & Shepherd, A. (2011). Ocean tides in the Weddell Sea: New observations on the Filchner-Ronne and Larsen C ice shelves and model validation. *Journal of Geophysical Research*, 116, C06006. <https://doi.org/10.1029/2011JC006949>
- Logan, L., Catania, G., Lavier, L., & Choi, E. (2013). A novel method for predicting fracture in floating ice. *Journal of Glaciology*, 59(216), 750–758. <https://doi.org/10.3189/2013JG12J210>
- Luckman, A., Jansen, D., Kulesa, B., King, E., Sammonds, P., & Benn, D. I. (2012). Basal crevasses in Larsen C Ice Shelf and implications for their global abundance. *The Cryosphere*, 6, 113–123. <https://doi.org/10.5194/tc-6-113-2012>
- MacAyeal, D. R. (1985). Tidal rectification below the Ross Ice Shelf, Antarctica. In S. S. Jacobs (Ed.), *Oceanology of the Antarctic continental shelf* (pp. 109–132). Washington, DC: American Geophysical Union.
- MacGregor, J. A., Anandakrishnan, S., Catania, G. A., & Winebrenner, D. P. (2011). The grounding zone of the Ross Ice Shelf, West Antarctica, from ice-penetrating radar. *Journal of Glaciology*, 57(205), 917–928.
- Makinson, K. (2002). Modeling tidal current profiles and vertical mixing beneath Filchner Ronne Ice Shelf, Antarctica. *Journal of Physical Oceanography*, 32(1), 202–215. [https://doi.org/10.1175/1520-0485\(2002\)032<0202:MTCPAV>2.0.CO;2](https://doi.org/10.1175/1520-0485(2002)032<0202:MTCPAV>2.0.CO;2)
- Makinson, K., Holland, P. R., Jenkins, A., Nicholls, K. W., & Holland, D. M. (2011). Influence of tides on melting and freezing beneath Filchner-Ronne Ice Shelf, Antarctica. *Geophysical Research Letters*, 38, L06601. <https://doi.org/10.1029/2010GL046462>
- Makinson, K., King, M. A., Nicholls, K. W., & Gudmundsson, G. H. (2012). Diurnal and semidiurnal tide-induced lateral movement of Ronne Ice Shelf, Antarctica. *Geophysical Research Letters*, 39, L10501. <https://doi.org/10.1029/2012GL051636>

- Makinson, K., & Nicholls, K. W. (1999). Modeling tidal currents beneath Filchner-Ronne Ice Shelf and on the adjacent continental shelf: Their effect on mixing and transport. *Journal of Geophysical Research*, 104(C6), 13,449–13,465.
- Marsh, O. J., Fricker, H. A., Siegfried, M. R., Christianson, K., Nicholls, K. W., Corr, Hugh F. J., & Catania, G. (2016). High basal melting forming a channel at the grounding line of Ross Ice Shelf, Antarctica. *Geophysical Research Letters*, 43, 250–255. <https://doi.org/10.1002/2015GL066612>
- Milillo, P., Rignot, E., Mouginot, J., Scheuchl, B., Morlighem, M., Li, X., & Salzer, J. T. (2017). On the short-term grounding zone dynamics of Pine Island Glacier, West Antarctica, observed with COSMO-SkyMed interferometric data. *Geophysical Research Letters*, 44, 10,436–10,444. <https://doi.org/10.1002/2017GL074320>
- Minchew, B. M., Simons, M., Riel, B., & Milillo, P. (2017). Tidally induced variations in vertical and horizontal motion on Rutford Ice Stream, West Antarctica, inferred from remotely sensed observations. *Journal of Geophysical Research: Earth Surface*, 122, 167–190. <https://doi.org/10.1002/2016JF003971>
- Mueller, R. D., Hattermann, T., Howard, S. L., & Padman, L. (2018). Tidal influences on a future evolution of the Filchner-Ronne Ice Shelf cavity in the Weddell Sea, Antarctica. *The Cryosphere*, 12(2), 453–476. <https://doi.org/10.5194/tc-12-453-2018>
- Mueller, R. D., Padman, L., Dinniman, M. S., Erofeeva, S. Y., Fricker, H. A., & King, M. A. (2012). Impact of tide-topography interactions on basal melting of Larsen C Ice Shelf, Antarctica. *Journal of Geophysical Research*, 117, C05005. <https://doi.org/10.1029/2011JC007263>
- Nye, J. F. (1953). The flow law of ice from measurements in glacier tunnels, laboratory experiments and the Jungfraufirn borehole experiment. *Proceedings of the Royal Society of London A: Mathematical, Physical and Engineering Sciences*, 219(1139), 477–489. <https://doi.org/10.1098/rspa.1953.0161>
- Padman, L., Erofeeva, S., & Joughin, I. (2003). Tides of the Ross Sea and Ross Ice Shelf cavity. *Antarctic Science*, 15(1), 31–40. <https://doi.org/10.1017/S0954102003001032>
- Padman, L., Fricker, H. A., Coleman, R., Howard, S., & Erofeeva, L. (2002). A new tide model for the Antarctic ice shelves and seas. *Annals of Glaciology*, 34(1), 247–254. <https://doi.org/10.3189/172756402781817752>
- Padman, L., King, M., Goring, D., Corr, H., & Coleman, R. (2003). Ice-shelf elevation changes due to atmospheric pressure variations. *Journal of Glaciology*, 49(167), 521–526. <https://doi.org/10.3189/172756503781830386>
- Padman, L., Siegfried, M. R., & Fricker, H. A. (2018). Ocean tide influences on the Antarctic and Greenland Ice Sheets. *Reviews of Geophysics*, 56, 142–184. <https://doi.org/10.1002/2016RG000546>
- Parizek, B. R., Christianson, K., Anandakrishnan, S., Alley, R. B., Walker, R. T., Edwards, R. A., et al. (2013). Dynamic (in)stability of Thwaites Glacier, West Antarctica. *Journal of Geophysical Research: Earth Surface*, 118, 638–655. <https://doi.org/10.1002/jgrf.20044>
- Pawlowicz, R., Beardsley, B., & Lentz, S. (2002). Classical tidal harmonic analysis including error estimates in MATLAB using T\_tide. *Computers & Geosciences*, 28(8), 929–937. [https://doi.org/10.1016/S0098-3004\(02\)00013-4](https://doi.org/10.1016/S0098-3004(02)00013-4)
- Pedley, M., Paren, J. G., & Potter, J. R. (1986). The tidal spectrum underneath Antarctic ice shelves. *Journal of Geophysical Research*, 91(C11), 13,001–13,009.
- Potter, J. R., Paren, J. G., & Pedley, M. (1985). Tidal behaviour under an Antarctic ice shelf. *British Antarctic Survey Bulletin*, 68, 1–18.
- Pritchard, H. D., Ligtenberg, S. R. M., Fricker, H. A., Vaughan, D. G., van den Broeke, M. R., & Padman, L. (2012). Antarctic ice-sheet loss driven by basal melting of ice shelves. *Nature*, 484(7395), 502–505. <https://doi.org/10.1038/nature10968>
- Rabus, B. T., & Lang, O. (2002). On the representation of ice-shelf grounding zones in SAR interferograms. *Journal of Glaciology*, 48(162), 345–356.
- Rack, F. R. (2016). Enabling clean access into Subglacial Lake Whillans: development and use of the WISSARD hot water drill system. *Philosophical Transactions of the Royal Society A: Mathematical, Physical and Engineering Sciences*, 374(2059), 20140305. <https://doi.org/10.1098/rsta.2014.0305>
- Ray, R. D. (2017). On tidal inference in the diurnal band. *Journal of Atmospheric and Oceanic Technology*, 34(2), 437–446. <https://doi.org/10.1175/JTECH-D-16-0142.1>
- Ray, R. D., & Egbert, G. D. (2004). The global S1 tide. *Journal of Physical Oceanography*, 34(8), 1922–1935. [https://doi.org/10.1175/1520-0485\(2004\)034<1922:TGST>2.0.CO;2](https://doi.org/10.1175/1520-0485(2004)034<1922:TGST>2.0.CO;2)
- Reddy, T. E., Holland, D. M., & Arrigo, K. R. (2010). Ross ice shelf cavity circulation, residence time, and melting: Results from a model of oceanic chlorofluorocarbons. *Continental Shelf Research*, 30(7), 733–742. <https://doi.org/10.1016/j.csr.2010.01.007>
- Reeh, N., Christensen, E. L., Mayer, C., & Olesen, O. B. (2003). Tidal bending of glaciers: A linear viscoelastic approach. *Annals of Glaciology*, 37(1), 83–89. <https://doi.org/10.3189/172756403781815663>
- Reeh, N., Mayer, C., Olesen, O. B., Christensen, E. L., & Thomsen, H. (2000). Tidal movement of Nioghalvfjærdsfjorden glacier, northeast Greenland: Observations and modelling. *Annals of Glaciology*, 31, 111–117. <https://doi.org/10.3189/172756400781820408>
- Reese, R., Gudmundsson, G. H., Levermann, A., & Winkelmann, R. (2018). The far reach of ice-shelf thinning in Antarctica. *Nature Climate Change*, 8(1), 53. <https://doi.org/10.1038/s41558-017-0020-x>
- Remondi, B. W. (1985). Global positioning system carrier phase: Description and use. *Bulletin Géodésique*, 59(4), 361–377. <https://doi.org/10.1007/BF02521069>
- Rignot, E. (1998). Hinge-line migration of Petermann Gletscher, north Greenland, detected using satellite-radar interferometry. *Journal of Glaciology*, 44(148), 469–476. <https://doi.org/10.3189/S0022143000001994>
- Rignot, E., Mouginot, J., & Scheuchl, B. (2011). Ice flow of the Antarctic Ice Sheet. *Science*, 333(6048), 1427–1430. <https://doi.org/10.1126/science.1208336>
- Rosier, S. H. R., & Gudmundsson, G. H. (2016). Tidal controls on the flow of ice streams. *Geophysical Research Letters*, 43, 4433–4440. <https://doi.org/10.1002/2016GL068220>
- Rosier, S. H. R., & Gudmundsson, G. H. (2018). Tidal bending of ice shelves as a mechanism for large-scale temporal variations in ice flow. *The Cryosphere*, 12(5), 1699–1713. <https://doi.org/10.5194/tc-12-1699-2018>
- Rosier, S. H. R., & Gudmundsson, G. H. (2020). Exploring mechanisms responsible for tidal modulation in flow of the Filchner-Ronne Ice Shelf. *The Cryosphere*, 14(1), 17–37. <https://doi.org/10.5194/tc-14-17-2020>
- Rosier, S. H. R., Gudmundsson, G. H., & Green, J. A. M. (2014). Insights into ice stream dynamics through modelling their response to tidal forcing. *The Cryosphere*, 8(5), 1763–1775. <https://doi.org/10.5194/tc-8-1763-2014>
- Rosier, S. H. R., Gudmundsson, G. H., & Green, J. A. M. (2015). Temporal variations in the flow of a large Antarctic ice stream controlled by tidally induced changes in the subglacial water system. *The Cryosphere*, 9(4), 1649–1661. <https://doi.org/10.5194/tc-9-1649-2015>
- Rosier, S. H. R., Gudmundsson, G. H., King, M. A., Nicholls, K. W., Makinson, K., & Corr, Hugh F. J. (2017). Strong tidal variations in ice flow observed across the entire Ronne Ice Shelf and adjoining ice streams. *Earth System Science Data*, 9(2), 849–860. <https://doi.org/10.5194/essd-9-849-2017>
- Rosier, S. H. R., Marsh, O. J., Rack, W., Gudmundsson, G. H., Wild, C. T., & Ryan, M. (2017). On the interpretation of ice-shelf flexure measurements. *Journal of Glaciology*, 63(241), 783–791. <https://doi.org/10.1017/jog.2017.44>

- Sassolas, C., Pfeffer, T., & Amadei, B. (1996). Stress interaction between multiple crevasses in glacier ice. *Cold Regions Science and Technology*, 24(2), 107–116. [https://doi.org/10.1016/0165-232X\(96\)00002-X](https://doi.org/10.1016/0165-232X(96)00002-X)
- Sayag, R., & Worster, M. G. (2011). Elastic response of a grounded ice sheet coupled to a floating ice shelf. *Physical Review E*, 84(3), 036111. <https://doi.org/10.1103/PhysRevE.84.036111>
- Sayag, R., & Worster, M. G. (2013). Elastic dynamics and tidal migration of grounding lines modify subglacial lubrication and melting. *Geophysical Research Letters*, 40, 5877–5881. <https://doi.org/10.1002/2013GL057942>
- Seroussi, H., & Morlighem, M. (2018). Representation of basal melting at the grounding line in ice flow models. *The Cryosphere*, 12(10), 3085–3096. <https://doi.org/10.5194/tc-12-3085-2018>
- Shepherd, A., Wingham, D., Payne, T., & Skvarca, P. (2003). Larsen ice shelf has progressively thinned. *Science*, 302(5646), 856–859. <https://doi.org/10.1126/science.1089768>
- Siegfried, M. R. (2015). Investigating Antarctic ice sheet subglacial processes beneath the Whillans Ice Plain, West Antarctica, using satellite altimetry and GPS (Thesis). San Diego, California: University of California, San Diego.
- Siegfried, M. R., & Fricker, H. A. (2018). Thirteen years of subglacial lake activity in Antarctica from multi-mission satellite altimetry. *Annals of Glaciology*, 59(76), 42–55. <https://doi.org/10.1017/aog.2017.36>
- Siegfried, M. R., Fricker, H. A., Carter, S. P., & Tulaczyk, S. (2016). Episodic ice velocity fluctuations triggered by a subglacial flood in West Antarctica. *Geophysical Research Letters*, 43, 2640–2648. <https://doi.org/10.1002/2016GL067758>
- Siegfried, M. R., Fricker, H. A., Roberts, M., Scambos, T. A., & Tulaczyk, S. (2014). A decade of West Antarctic subglacial lake interactions from combined ICESat and CryoSat-2 altimetry. *Geophysical Research Letters*, 41, 891–898. <https://doi.org/10.1002/2013GL058616>
- Siegfried, M. R., Medley, B., Larson, K. M., Fricker, H. A., & Tulaczyk, S. (2017). Snow accumulation variability on a West Antarctic ice stream observed with GPS reflectometry, 2007–2017. *Geophysical Research Letters*, 44, 7808–7816. <https://doi.org/10.1002/2017GL074039>
- Sun, S., Hattermann, T., Pattyn, F., Nicholls, K. W., Drews, R., & Berger, S. (2019). Topographic shelf waves control seasonal melting near Antarctic Ice Shelf grounding lines. *Geophysical Research Letters*, 46, 9824–9832. <https://doi.org/10.1029/2019GL083881>
- Thomas, R. H. (2007). Tide-induced perturbations of glacier velocities. *Global and Planetary Change*, 59(1), 217–224. <https://doi.org/10.1016/j.gloplacha.2006.11.017>
- Thompson, J., Simons, M., & Tsai, V. C. (2014). Modeling the elastic transmission of tidal stresses to great distances inland in channelized ice streams. *Cryosphere*, 8(6), 2007–2029.
- Tsai, V. C., & Gudmundsson, G. H. (2015). An improved model for tidally modulated grounding-line migration. *Journal of Glaciology*, 61(226), 216–222. <https://doi.org/10.3189/2015JoG14J152>
- Tulaczyk, S., Mikucki, J. A., Siegfried, M. R., Priscu, J. C., Barcheck, C. G., Beem, L. H., et al. (2014). WISSARD at subglacial Lake Whillans, West Antarctica: Scientific operations and initial observations. *Annals of Glaciology*, 55(65), 51–58. <https://doi.org/10.3189/2014AoG65A009>
- van der Veen, C. J. (1998). Fracture mechanics approach to penetration of bottom crevasses on glaciers. *Cold Regions Science and Technology*, 27(3), 213–223. [https://doi.org/10.1016/S0165-232X\(98\)00006-8](https://doi.org/10.1016/S0165-232X(98)00006-8)
- van der Veen, C. J. (2016). Basal buoyancy and fast-moving glaciers: In defense of analytic force balance. *The Cryosphere*, 10(3), 1331–1337.
- Walker, R. T., Parizek, B. R., Alley, R. B., Anandakrishnan, S., Riverman, K. L., & Christianson, K. (2013). Ice-shelf tidal flexure and subglacial pressure variations. *Earth and Planetary Science Letters*, 361, 422–428. <https://doi.org/10.1016/j.epsl.2012.11.008>
- Washam, P., Nicholls, K. W., Mnchow, A., & Padman, L. (2019). Summer surface melt thins Petermann Gletscher Ice Shelf by enhancing channelized basal melt. *Journal of Glaciology*, 65, 662–674. <https://doi.org/10.1017/jog.2019.43>
- Werder, M. A., Hewitt, I. J., Schoof, C. G., & Flowers, G. E. (2013). Modeling channelized and distributed subglacial drainage in two dimensions. *Journal of Geophysical Research: Earth Surface*, 118, 2140–2158. <https://doi.org/10.1002/jgrf.20146>
- Wild, C. T., Marsh, O. J., & Rack, W. (2018). Unraveling InSAR observed Antarctic Ice-Shelf flexure using 2-D elastic and viscoelastic modeling. *Frontiers in Earth Science*, 6, 28. <https://doi.org/10.3389/feart.2018.00028>
- Winberry, J. P., Anandakrishnan, S., Alley, R. B., Wiens, D. A., & Pratt, M. J. (2014). Tidal pacing, skipped slips and the slowdown of Whillans Ice Stream, Antarctica. *Journal of Glaciology*, 60(222), 795–807. <https://doi.org/10.3189/2014JoG14J038>
- Yeager, B. A. (2018). Moving mesh finite element modeling of ocean circulation beneath ice shelves (Doctoral Thesis). Imperial College London. <https://doi.org/10.25560/73697>
- Zoet, L. K., Anandakrishnan, S., Alley, R. B., Nyblade, A. A., & Wiens, D. A. (2012). Motion of an Antarctic glacier by repeated tidally modulated earthquakes. *Nature Geoscience*, 5(9), 623–626. <https://doi.org/10.1038/ngeo1555>